University of Twente

Master Thesis Applied Mathematics

Numerical calculation of magnetoresistance in a thin-film Bi_2Te_3 topological insulator

Multiscale Modeling and Simulation
Interfaces and Correlated Electron systems

Author:
D.R. de Ruiter
s1086162

Graduation committee
prof. dr. ir. B.J. Geurts
dr. R.M.J. van Damme
DI M.P. Stehno, PhD

External member
prof. dr. ir. A. Brinkman

July 4, 2016

Abstract

The magnetoresistance is calculated for thin-film Bi_2Te_3, a topological insulator. As a first step, the band structure is obtained through self-consistently solving a set of coupled Schrödinger-Poisson equations within the numerical package NEMO5. The Schrödinger equation is solved using a tight-binding Hamiltonian. The Poisson equation is solved by a FEM routine. As a next step, the group velocities, effective masses and wave function overlaps are obtained from the band structure. With these results, the conductivity is calculated by solving the linearized Boltzmann equation. A nonzero electrostatic potential is fixed on one of the surfaces, to mimic gating and the presence of charged adsorbates on the surface. Effects of a magnetic field on the band structure and on the alignment of the spin are investigated. The resulting energy shifts of the bands are smaller than observed in literature. The calculations for the magnetoresistance do not predict positive, linear magnetoresistance when only topological surface states contribute to the transport. When bulk conduction bands contribute as well, positive magnetoresistance is observed.

Contents

1. Introduction

Topological insulators have been a subject of interest in recent years. The term 'topological' refers to the fact that certain fundamental properties of such materials are insensitive to smooth changes in material parameters[1]. Like (semi)conductors, topological insulators have a band gap separating the valence and conduction bands. In topological insulators, however, this gap is spanned by the so-called *Dirac cone*, which consists of states bound to the surfaces of the material.

Such a material can be conducting on the surfaces while being an insulator in the bulk. Practical applications are still explored, but the use of 'Majorana particles' for quantum computers is regularly mentioned in literature.

Topological insulators such as Bi_2Te_3[2] and Bi_2Se_3[3] have been shown to exhibit positive linear magnetoresistance for transverse magnetic fields. In cited literature, it is suggested that the states in the Dirac cone play an important role in this effect. It would, however, be optimistic to say that the effect is fully understood. A model that can replicate the specific magnetoresistance behavior can, hopefully, give more insight in the involved mechanisms.

The rest of this chapter gives a general introduction to the unit cell of Bi_2Te_3, and to important concepts in solid state physics, specifically the tight-binding model, topological insulators and magnetoresistance.

1.1. Bismuth Telluride unit cell

Bismuth telluride is built up from layers of identical atom types. Figure 1.2 shows the unit cell, its top view and the layer structure. There are two types of inequivalent tellurium atoms. They are distinct due to their different nearest neighbors: Te1 has another Te1 and a Bi atom, while Te2 has two Bi atoms as its neighbors.

The unit cell is, technically speaking, a rhombohedron with lattice vectors $t_{1..3}$ in figure 1.2. Here, it will be described using a hexagonal unit cell with the lattice vectors in figure 1.1a, top view. Their lengths are 3.0487 nm in the C-direction and 0.4383 nm in the A-B-plane. Those last two vectors make an angle of 120°. A different choice for the lattice vectors could have resulted in a smaller unit cell. In section 2.1.1 this choice is explained.

During the calculations, integrals over the lattice will be calculated. A summation over all positions in the lattice in real space is equivalent to summing over the wave vectors in just the first Brillouin zone. The corresponding reciprocal lattice vectors are obtained by

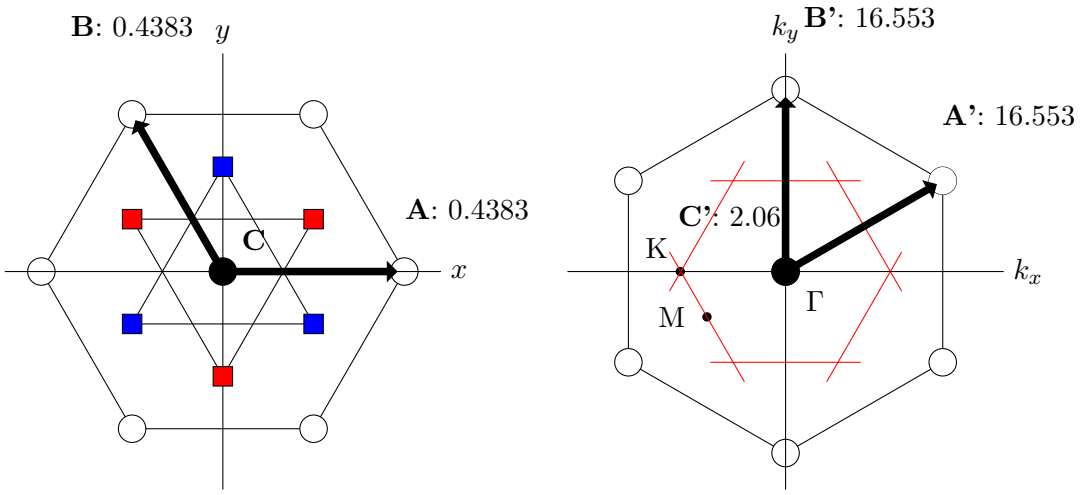

(a) real space, lengths in nm

(b) reciprocal space, lengths in nm^{-1}

Figure 1.1.: Top view of unit cell

the usual transformation:

$$A' = 2\pi \frac{B \times C}{A \cdot (B \times C)} \tag{1.1}$$

$$B' = 2\pi \frac{C \times A}{B \cdot (C \times A)} \tag{1.2}$$

$$C' = 2\pi \frac{A \times B}{C \cdot (A \times B)} \tag{1.3}$$

which is just the Fourier transform of the real space Bravais lattice. The reciprocal vectors are shown in figure 1.1b. The first Brillouin zone is the primitive unit cell in reciprocal space and is encapsulated by the red lines. Its 'volume' is $2.45 \times 10^{29}\,\mathrm{m}^{-3}$. Points of high symmetry include Γ, M and K. Band structure plots will often sweep through the first Brillouin zone along the directions K-Γ-M.

This thesis will focus on a specific Bi_2Te_3 system. It consists of fifteen quintuple layers (QL) of Bi_2Te_3 on top of a substrate of strontium titanate ($SrTiO_3$). A quintuple layer is approximately one nanometer thick. The thin-film is grown along the crystallographic C-axis, which is directed along the z-axis of the model. Throughout this thesis, it is assumed that the system is an infinite slab in the A-B-plane, which is modeled by periodic boundary conditions along the x- and y- axes. Electrons are tightly confined in the z-direction. This causes a large quantization energy for the out-of-plane axis. Therefore, states with wave vector component k_z unequal to zero are neglected. The surface states in Bi_2Te_3 result from strong spin-orbit coupling.

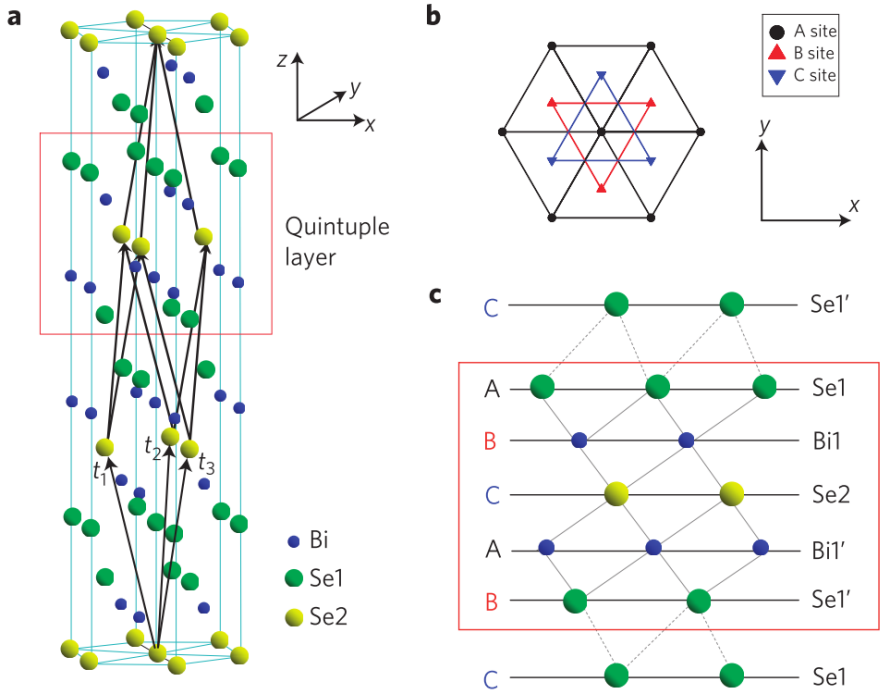

Figure 1.2.: Bi_2Se_3 unit cell, from Zhang et al. [4]. The Bi_2Te_3 unit cell looks similar after substituting Te for Se.

1.2. Solid state physics

This section will give an introduction to some concepts of solid-state physics that are used in this thesis. Solid state physics is a branch of physics that studies various properties of solids. Quantum mechanics is one of the methods used to predict those properties, using the atomistic structure. The atoms are organized in a periodic structure, or crystal. This idealized picture enables the use of useful tools as the Bloch theorem.

1.2.1. Time-independent Schrödinger equation

The Schrödinger equation is a tool to describe the electronic structure of a system. Solving this equation is the main objective in theoretical solid state physics and quantum mechanics in general. For a system at rest or describing a periodic motion, the time-independent Schrödinger equation can be used. In Dirac notation it is written as

$$\mathcal{H} |\psi_n\rangle = E_n |\psi_n\rangle . \tag{1.4}$$

This is the eigenvalue problem for the Hamiltonian $\mathcal{H}$. The Hamiltonian is a Hermitian operator on a Hilbert space, corresponding to the energy of a system. To find an expression for it, one must thus use a physical model that describes the energy for the system of interest. The eigenvalues of the Hamiltonian are the allowed energies of a system. For a free particle, the spectrum is continuous, so that it can have any energy.

For electrons that are confined by a potential, as is the case in a solid, these energies are quantized.

For each eigenvalue E_n there is an accompanying eigenvector $|\psi_n\rangle$. A specific $|\psi_a\rangle$ describes one of the allowed states of a system and is often called an eigenstate. What exactly such a state is, depends on the system. The dimensionality of the Hilbert space depends on the physical model that was used to construct the Hamiltonian. An example of a two-dimensional Hilbert space is the spin state of an electron. A measurement can only result in spin 'up' or 'down'. The two eigenvectors are $\begin{pmatrix}1\\0\end{pmatrix}$ for up and $\begin{pmatrix}0\\1\end{pmatrix}$ for down and these two vectors form an orthogonal basis for the space. A linear combination of the two can describe any state of the system.

The problem becomes infinite dimensional when also the position of the electron is taken in account. Consider the one-dimensional infinite potential well. In this case, the state $|\phi\rangle$ is described by the wave function. When squared, it gives the probability density of finding the electron at certain x: it is a continuous and differentiable function $f : \mathbb{R} \to \mathbb{C}$. An orthogonal basis is formed by the Fourier series, hence an infinite number of $|\psi_n\rangle$ are needed.

1.2.2. Tight-binding Hamiltonian

Consulted literature for this section is Ashcroft and Mermin [5, Chapter 10]. A Hamiltonian must be chosen that captures the essential features of the physical system. Here, a tight-binding Hamiltonian will be used. The tight-binding approach is suitable when the electrons in the system remain tightly bound to the atom to which they belong. They have little interaction with surrounding atoms and their electrons. Still, electrons are allowed to hop to neighboring atoms. It is then reasonable to assume that the wave functions of the electrons look a lot like the wave functions of a free atom. The total Hamiltonian is just the sum of the Hamiltonian for all the separate atoms plus a perturbation:

$$\mathcal{H}(r) = \sum_{R_n} (r - R_n) + \Delta U(r). \tag{1.5}$$

However, this perturbation is small enough to assume that a wave function that solves the Hamiltonian is of the shape

$$\psi(r) = \sum_{m,R_n} b_m(R_n)\psi_m(r - R_n), \tag{1.6}$$

where $\psi_m(r)$ are the atomic orbitals. The wave function is thus given by a linear combination of the atomic orbitals.

On the other hand, there is the Bloch theorem, which states that the eigenstates in a crystal obey the relation

$$\psi(r + R_l) = e^{\mathrm{i}k\cdot R_l}\psi(r). \tag{1.7}$$

This theorem is very general and says that the wave functions in an infinite crystal have a certain periodicity in the lattice. By combining these two equations, one can derive

that the general shape of a solution to the tight-binding Hamiltonian is

$$\psi(r) = \frac{1}{\sqrt{N}} \sum_{m,R_n} e^{\mathrm{i}k\cdot R_n} \psi_m(r - R_n), \tag{1.8}$$

with ψ_m atomic orbitals and R_n the positions of the atoms in real space. The indices m and n run over the orbitals and atoms, respectively. A finite number of both is used, which reduces the Hilbert space to a $m_{\mathrm{tot}} \cdot n_{\mathrm{tot}}$ dimensional space. The Hamiltonian is thus a matrix. With this shape of the wave equation, it is possible to derive a general expression for the energies, or eigenvalues of the Hamiltonian:

$$E_n(k) = \int \psi^*(r) \mathcal{H} \psi(r) d^3r = f(\beta_m, \gamma_m, \alpha_m). \tag{1.9}$$

where the *tight-binding parameters* are given by

$$\beta_{m,m} = -\int \psi_m^*(r) \Delta U(r) \psi_m(r) d^3r \tag{1.10}$$

$$\gamma_{m,l} = -\int \psi_m^*(r) \Delta U(r) \psi_l(r - R_n) d^3r \tag{1.11}$$

$$\alpha_{m,l} = \int \psi_m^*(r) \psi_l(r - R_n) d^3r, \tag{1.12}$$

which are the atomic energy shift, the inter atomic matrix element and the overlap integral, respectively. These parameters are used to fill the Hamiltonian matrix together with information about the geometric structure of the material to model. The tight-binding parameters have to be known in advance. In this case, the parameters were obtained by fitting the band structure to a density functional theory (DFT) calculation by Lee and Allmen [6].

1.2.3. Band structure

Some textbook problems in quantum mechanics are easily solved analytically, such as the infinite potential well and the harmonic oscillator. Most interesting problems have no exact solution and need to be solved numerically. The Hamiltonian for an n-dimensional problem is a n×n matrix, so solving an infinite dimensional system is problematic. Such systems are often solved by taking a finite part of the system and invoking periodic boundary conditions. The problem is then reduced to a finite dimensional version with a finite number of solutions.

In the tight binding Hamiltonian, the wave vector $\mathbf{k}$ appears. For an electron in a crystal, it is related to its crystal momentum by

$$\mathbf{p}_{\mathrm{crystal}} = \hbar \mathbf{k}. \tag{1.13}$$

Since the wave vector appears in the Hamiltonian, the eigenvectors will depend on it as well. An n-dimensional system has n eigenvectors, which all continuously depend on $\mathbf{k}$.

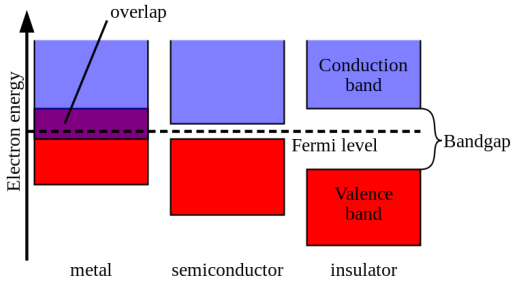

(a) Band structure diagram of conventional materials

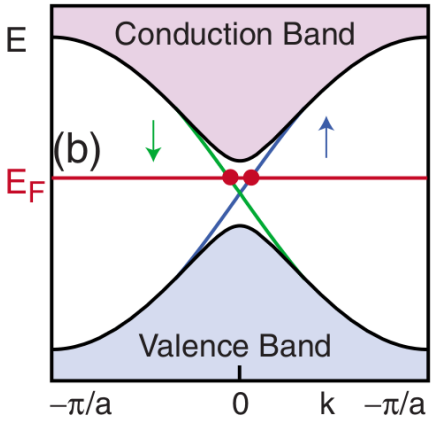

(b) Idealized band structure of a topological insulator, from Hasan and Kane [1]

Figure 1.3.: Schematic band structures

The eigenstates and energies can now be denoted as $|\psi_{n,k}\rangle$ and $E_{n,k}$. Both are periodic in $\mathbf{k}$ with a periodicity of $2\pi/A'$, with A' the appropriate reciprocal lattice vector.

It is common in solid state physics to plot the dispersion relation: the eigenenergies as a function of the wave vector. Since the latter one is a three dimensional vector it is common to plot a range of $\mathbf{k}$ values between points of high-symmetry in the Brillouin zone. For each $\mathbf{k}$ there are as many energies as the dimension of the Hamiltonian. The energies vary continuously with $\mathbf{k}$ so that when the resolution is high enough, smooth bands appear. These plots are appropriately named *band structure* plots. Note that the resolution is something fundamental: the Bloch waves must fit in the lattice. The wave vector is inversely proportional to an integer times one of the lattice constants, and its minimum value is limited by the size of the system. For a 'real' system the band structure becomes continuous due to the large system size.

Band gap

A schematic of three different band diagrams is shown in figure 1.3a. The bands are drawn as continuous regions but are in reality a very large number of discrete dots. There are more states available than electrons, so some bottom portion of the band structure will be filled with electrons. The average number of electrons in a state depends on its energy and is given by the Fermi-Dirac distribution. At zero temperature, the Fermi-Dirac distribution is a step function. The value of this function is one below the electrochemical potential, or *Fermi level*, and zero above it. Thus, all states with an energy below the Fermi level are filled with exactly one electron. Bands below the Fermi level are called valence bands, bands above it are conduction bands.

For metals, the Fermi level lies in the conduction band. This means that in a metal, electrons around the Fermi level can make an infinitesimally small jump to another,

unoccupied state. The electrons are said to be in a metallic state. Such electrons can move around, explaining why metals conduct electricity.

Insulators have gap between the valence and conduction bands, with the Fermi level in between. There are no allowed states in the gap. Electrons would have to gain a lot of energy to jump to a free state in the conduction band. All electrons are stuck where they are, and no electrical conduction is possible.

Insulators with a small band gap are called semiconductors. They are insulating at zero temperature. At higher temperatures, an electron might be able to jump from the valence band to the conduction band with the help of thermal energy, following from the Fermi-Dirac distribution. The semiconductor then becomes conducting. The Fermi level can be shifted by adding or subtracting electrons from the system, also resulting in an increase of conductivity. One way to do this is through gating, which means that an electric field is invoked at a surface of the semiconductor.

Bi_2Te_3 is a narrow gap semiconductor, with a band gap of ± 0.2 eV.

1.3. Topological insulators

Bi_2Te_3 is a topological insulator, which is characterized by a full insulating gap in the bulk and gapless surface states which are protected by time-reversal symmetry[7]. The dispersion of the surface states spans the usual gap between the valence and the conduction bands in a semiconductor. A schematic band diagram is shown in figure 1.3b. The states that span the gap are referred to as the 'Dirac cone', because of the linear dispersion of the topological surface states. An electron which occupies a surface state is bound to a surface in real space. The surface states are metallic. Therefore, if the Fermi level is placed in the band gap, a topological insulator is insulating in the bulk and conducting on its surfaces. The direction of the spin of these states is tightly coupled to their momentum.

The surface states in Bi_2Te_3 exist as a result of strong spin-orbit coupling[4]. Spin-orbit coupling enters the Hamiltonian as an extra term

$$H_{\mathrm{SO}} = \alpha_{\mathrm{SO}}(\mathbf{L} \cdot \mathbf{S}), \tag{1.14}$$

for orbital angular momentum L and spin angular momentum S. The parameter α_{SO} determines the strength of the coupling. In the tight-binding Hamiltonian matrix, spin-orbit coupling appears as an extra tight-binding parameter between the different p orbitals of single atoms.

The strong spin-orbit coupling causes band inversion, which drives the system in a topological insulator phase. Specifically, the p orbitals invert in Bi_2Te_3. This process is shown in figure 1.4, which starts with the separate p orbitals. The first stage (I) shows the effect of chemical bonding between bismuth and tellurium within a quintuple layer. The bonding results in five hybridized orbitals. In stage (II) the crystal-field splitting is turned on. The effect is caused by the static electric field of the neighboring atoms. It breaks the degeneracy of some hybridized orbitals, bringing a bismuth orbital and a tellurium orbital closer together in energy. The spin-orbit coupling is turned on in

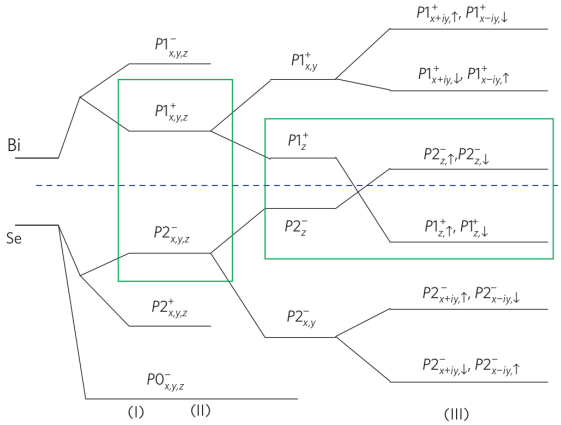

Figure 1.4.: Schematic diagram of the evolution from the atomic $p_{x,y,z}$ orbitals of Bi_2Te_3 at the gamma point. The diagram looks qualitatively the same for Bi_2Te_3. Image from Zhang et al. [4]

stage (III). The energy of the bismuth orbital is further decreased, while the energy of the tellurium orbital is increased, causing them to cross. As a result, the system is topologically non-trivial.

1.3.1. Surface states

This subsection will qualitatively discuss some mechanisms to create protected surface states. The goal is not to fully explain the workings of a three dimensional topological insulator, but rather to get a feeling for how the surface states behave. Consulted literature includes Kane and Moore [8], which is also the source of the images. Lecture notes for the course 'Advanced Condensed Matter Physics', by Kai Sun at the University of Michigan, were used as well[9].

Quantum Hall effect

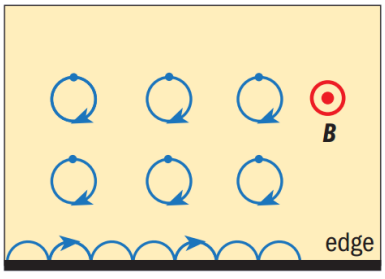

Different quantum mechanical effects can cause protected surface states to exist. They come with different types of protection. A two dimensional electron system can be in the *quantum Hall state*, which can only occur in strong magnetic fields for sufficiently low temperatures. Instead of surface states, such a system has one dimensional edge states. These are topologically protected, meaning that they are unaffected by any type of local impurities. Transport along the edges is dissipationless. On each edge, the current flows in only one direction. Spin and momentum are locked together, thus on each edge the current is spin polarized. To scatter back on an impurity, an electron would have to change its momentum by 180 degrees and, thus, flip

its spin. The probability of such an event is zero since the two quantum states have no overlap. The quantum Hall state can only exist in two dimensions.

Quantum spin Hall effect

The quantum spin Hall effect is another way to create protected states and it works in both, two and three dimensions; for now, consider a two dimensional system. Rather than an external magnetic field, strong spin-orbit coupling drives this mechanism. Magnetic fields are produced internally by this coupling and, loosely speaking, they play the role of the external field of the quantum Hall effect. Spin up and spin down particles feel this field in opposite directions, which causes two edge states to exist at each edge. These states have opposite spin polarization and opposite velocity. As no net charge is transported, it is appropriate to speak of 'spin currents'. The edge states in a quantum spin Hall state are *not* topologically protected. Rather, they are protected as long as time-reversal symmetry is not broken. One way to break time-reversal symmetry is by applying a magnetic field. Magnetic impurities, which do not affect the quantum Hall state, can also destroy the edge states of the quantum spin Hall state. Transport is dissipationless, for the same reasons as for the quantum Hall state.

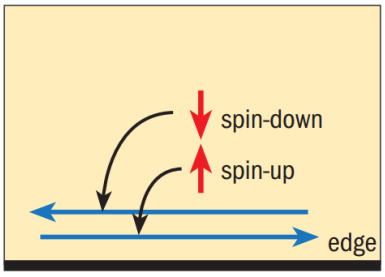

The quantum spin Hall state can be generalized to three dimensions. In this case, the system contains surface states, which means that current can flow in all directions in the x–y plane. Spin and momentum are still locked, a state cannot backscatter to the state with opposite momentum. It can, however, scatter to states with close-by momenta. Transport in a quantum spin Hall state is, therefore, not dissipationless, but the spin-orbit coupling certainly reduces resistivity.

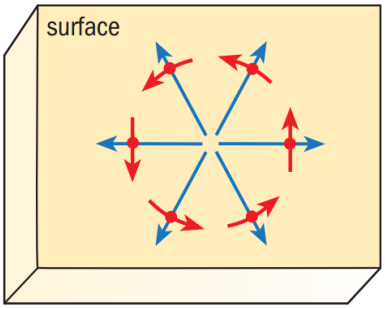

A three dimensional topological insulator behaves similar to the quantum spin Hall state. The resistivity is reduced in the same manner. A Dirac appears in the band structure, with states that are bound to one of the surfaces. The spin of these states is perpendicular to their momentum. The surface states are not protected by topology. They are only protected if time-reversal symmetry is not broken. Therefore, the Dirac cone can be destroyed by applying a magnetic field or by magnetic impurities.

1.4. Magnetoresistance

Electrical conductivity σ is defined to be the proportionality factor between the electric field $\boldsymbol{\mathcal{E}}$ at a point in a material and the current density $\mathbf{j}$ that it induces. This relation is

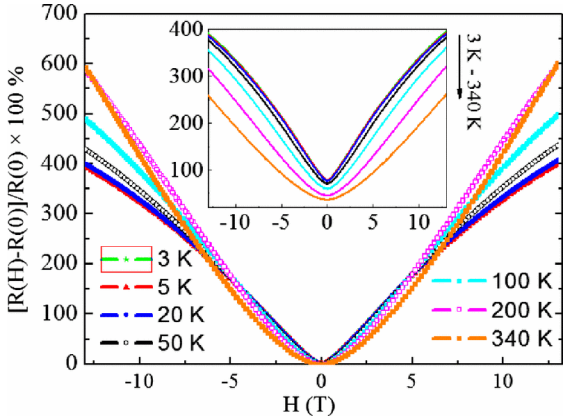

Figure 1.5.: Field dependence of the transverse magnetoresistance (inset) and the MR ratio between 3 and 340 K for a 20 QL Bi_2Te_3 nanosheet, from Wang et al. [2].

given by

$$\mathbf{j} = \sigma \boldsymbol{\mathcal{E}}. \tag{1.15}$$

The conductivity is a tensor for systems of more than one dimension. For the thin-film considered in this thesis it is a 2x2 matrix. The resistivity tensor is the inverse of the conductivity tensor, defined as

$$\boldsymbol{\rho} = \begin{bmatrix} \rho_{xx} & \rho_{xy} \\ \rho_{yx} & \rho_{yy} \end{bmatrix} = \boldsymbol{\sigma}^{-1}. \tag{1.16}$$

For some materials, the resistivity changes when an external magnetic field is applied. This magnetic field-dependent resistivity is the magnetoresistance. In this thesis the magnetic field is applied perpendicularly to the current, so that the *transverse* magnetoresistance is considered. Measurements of the resistivity of thin-film Bi_2Te_3 show a positive linear correlation with the magnitude of a perpendicularly applied magnetic field, see figure 1.5.

Wang et al. [2] claim that the linear magnetoresistance is mainly due to the topological surface states. He et al. [3] make a similar claim for topological insulator Bi_2Se_3 thin-films. However, Leusink et al. [10] observe large magnetoresistance in the conducing bulk state of Bi_2Te_3. They propose a mechanism for magnetoresistance that is applicable to a wide class of systems with spin-orbit coupling. The mechanism could explain magnetoresistance for surface states, which have strong spin-orbit coupling, and for bulk states, which have weaker spin-orbit coupling.

In absence of a magnetic field, the spin and momentum of a state with strong spin-orbit coupling are perpendicular. This makes it improbable for an electron to scatter to a state with opposite momentum, see figure 1.6. This reduction in backscattering results in a lower resistivity. Assume that the surfaces of the thin-film lies in the x–y plane. When a magnetic field is switched on along the z-axis, the spins are forced to align (up

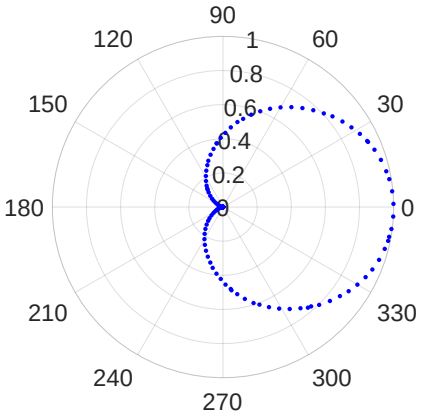

Figure 1.6.: Angular distribution of the wave function overlap for a state in the Dirac cone. The figure is a result of calculations in later chapters.

or down) with this field. Spins of states which were previously orthogonal, i.e., the spins were pointing in opposite directions in the x–y plane, now have a finite overlap. The resistivity of the material increases in the magnetic field.

1.5. Project goal

The goal of this project is to calculate the magnetoresistance in bismuth telluride, Bi_2Te_3. Measurements have shown that the magnetoresistance in comparable Bi_2Te_3 samples is positive and linear. This positive linear relation is sometimes attributed to transport by the topological surface states. However, bulk states might be involved as well.

The project was carried out in two phases. First it is necessary to obtain the band structure. This is be done in part I, using a self-consistent Schrödinger-Poisson calculation. The band structure is used to determine which states contribute to transport for a certain Fermi level. The group velocity, effective mass and overlap to other states are obtained as well. The second step is to use these data to calculate the magnetoresistance. This is done in part II, using the linearized Boltzmann equation. Pure surface state transport is compared with mixed transport by topological surface states and bulk states. Finally, part III gives the conclusion and outlook.

Part I.

Band structure

2. Method

The first step towards obtaining a model for the magnetoresistance is solving the Schrödinger-Poisson equation for the system. As mentioned before, a tight-binding model will be applied to do so. While the underlying principles of the method are not very hard to grasp, writing a stable code is a complex task. Therefore, it was decided to make use of the numerical package NEMO5 [11]. NEMO5 also includes a FEM solver for the Poisson calculations, and it can compute inner products to obtain wave function overlaps. These are used in the calculation of the relaxation time, which is required to calculate the magnetoresistance.

2.1. Model in NEMO

2.1.1. Unit cell

To build the Hamiltonian, information about the geometrical structure is required. NEMO5 uses a unit cell consisting of three quintuple layers, as depicted in figure 2.1. It is, therefore, as thick as the entire unit cell in figure 1.2; only after fifteen layers does the exact pattern of atoms repeat itself. This convention is chosen, because it allows the use of two lattice vectors in the x–y plane and one along the z-axis, rather than angled ones. As a consequence, the thickness of the thin-film can only be chosen to be a multiple of three quintuple layers. In the following, a system is considered which is 15 QL thick. Periodic boundary conditions are assumed in the x–y plane in order to keep the computational cost reasonable. In practice, this means that each atom is connected to each of its neighbors six times, with a sixty-degree offset between the bonds.

Notice that the surfaces can be terminated by one bismuth layer and one tellurium layer, or by two tellurium layers, depending on where the unit cell is defined to start. The asymmetrical case is less stable because of an intrinsic potential difference between the two surfaces. It does not occur in nature. Therefore, the symmetric is considered.

2.1.2. Tight-binding basis states

The tight-binding implementation in NEMO5 uses the $sp^3d^5s^*$ model for the atomic orbitals. The tight-binding parameters were obtained by fitting the band structure to the results of a first-principles calculation[6]. Because spin-orbit coupling is the driving mechanism for the topological surface states in Bi_2Te_3, spin is included as well. Each orbit appears both in a spin-up and a spin-down configuration. A general state of an isolated atom, thus, has twenty components:

$$|\psi\rangle = \big|s\uparrow, p_x\uparrow, p_y\uparrow, p_z\uparrow, d_{xy}\uparrow, d_{yz}\uparrow, d_{zx}\uparrow, d_{x^2-y^2}\uparrow, d_{z^2}\uparrow, s^*\uparrow, s\downarrow, \ldots\big\rangle\,. \quad (2.1)$$

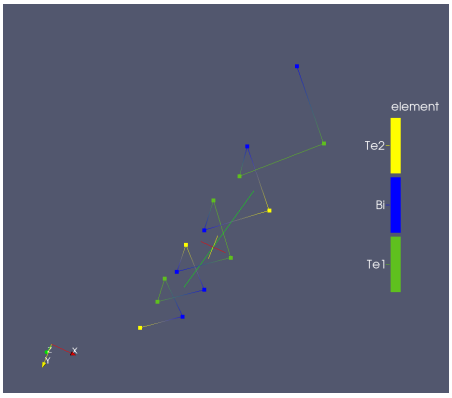

Figure 2.1.: The unit cell in NEMO5

A unit cell contains fifteen atoms which means that each quintuple layer consists of five atoms. For the fifteen quintuple layer system this means that 75 atoms are considered. The Hamiltonian and its eigenvectors are thus

$$\mathcal{H} \in \mathbb{C}^{n\times n}, \qquad |\psi\rangle \in \mathbb{C}^{n}, \tag{2.2}$$

where

$$n = 20 \text{ orbits} \times \text{no. of QL} \times 5 \text{ atoms per QL}. \tag{2.3}$$

Specifically, NEMO5 will solve an eigenvalue problem of dimension 1500 for each k-point. Since this is done numerically, the Hamiltonian has to be rebuilt for each k-point as well.

2.1.3. Spin

For overlap calculations, it is not necessary to extract spin data for the states as that is a simple matter of taking an inner product. All spin information is taken into account implicitly. Extraction of spin expectation values is still useful to visualize the effect of strong spin-orbit coupling and to see whether the surface states indeed have opposite spin currents. A general spin state can be described as $\begin{pmatrix} a \\ b \end{pmatrix}$, with expectation values

$$\langle S_x \rangle = \frac{\hbar}{2}(a^* b + b^* a) \tag{2.4}$$

$$\langle S_y \rangle = \mathrm{i}\frac{\hbar}{2}(b^* a - a^* b) \tag{2.5}$$

$$\langle S_z \rangle = \frac{\hbar}{2}(|a|^2 - |b|^2). \tag{2.6}$$

For a single atom, the output of NEMO5 is structured

$$|a|^2 = \langle \psi_i | \psi_i \rangle , \qquad i = 1 \ldots 10 \tag{2.7}$$

$$|b|^2 = \langle \psi_i | \psi_i \rangle , \qquad i = 11 \ldots 20 \tag{2.8}$$

$$b^* a = \langle \psi_i | \psi_{i+10} \rangle , \qquad i = 1 \ldots 10 \tag{2.9}$$

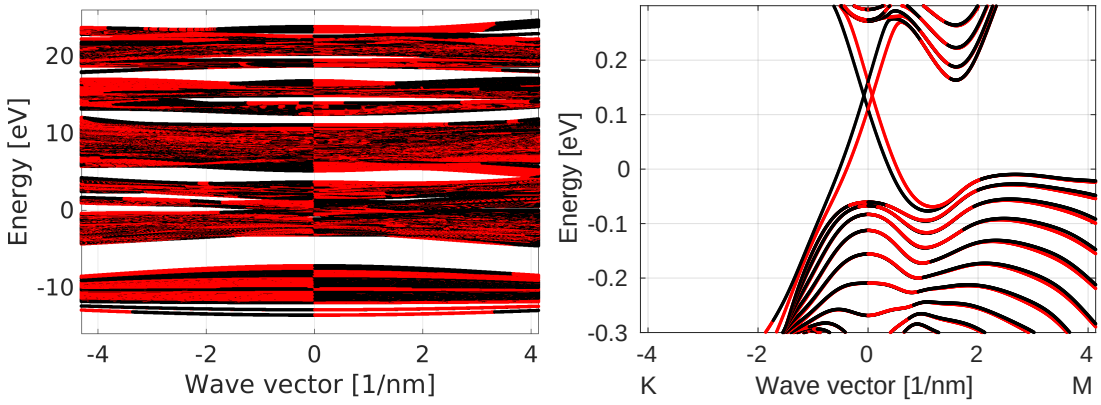

(a) full (b) cropped

Figure 2.2.: The band structure for a Schrödinger calculation

from which the expectation values can be calculated easily. For the Bi_2Te_3 model, the index i runs over (20 orbitals) x (15 atoms/u.c.) x (5 unit cells).

2.1.4. 2D k-space grid

For a typical band structure plot, k-space sampling is done along a line. Usually, k_z is set to zero and a certain path is chosen in the k_x–k_y plane. For the magnetoresistance calculations, however, all contributing states on the Fermi *surface* must be found. It is, therefore, necessary to mesh the entire k_x–k_y plane plane while, again, k_z is set to zero. The grid points can lie along the reciprocal vectors, although they are not normalized. Another option is to use Cartesian coordinates to create a square grid. Building the grid in such a way that it just includes all bands crossing the surface, obviously, results in the best resolution at lowest cost. Because the unit cell, and thus the contours of the bands at a certain energy level, are approximately hexagonal, a coarse grid will result in a distorted slice. Meanwhile, the computational cost of the Schrödinger calculation increases linearly with the number of k-points.

2.2. Schrödinger solver

A first attempt to solve the Schrödinger equation results in the band structure of figure 2.2b. The positive x-axis covers half of one of the reciprocal vectors, in the direction of the M points in the Brillouin zone. The negative x-axis shows points towards the K point. Notice that this is a cropped plot. Most of the valence and conduction bands are not shown here because they are not relevant for the low-energy physics that are studied here. Figure 2.2a shows the full band structure. It is possible to avoid calculating all these obsolete solutions to the eigenvalue problem by using an iterative Krylov method. In practice, this was not faster than the direct solver while sometimes problems with convergence arose. All results in this paper were derived using direct eigenvalue solvers.

The most eye-catching aspect of the band structure is the double Dirac cone. One can distinguish two separate cones; one for each surface. Experimentally this is not observed. One should keep in mind that a Schrödinger calculation without its Poisson counterpart is hardly physical, for it neglects the electrostatics of the problem. It turns out that indeed a self-consistent approach makes the bands coincide.

Spin information is represented by the coloring. A red state has a positive expectation value for its spin component in the x-direction; a black state a negative one. This explains the symmetry around the gamma point, caused by spin-momentum locking. Compare with figure 2.4f, which shows the spin-x and spin-y expectation values from a top view for $E = 0$.

2.2.1. Derivatives

For the magnetoresistance calculations, it is necessary to calculate first- and- second order derivatives of the energy in the k_x–k_y plane. Since the grid is discrete this is done using a straightforward finite difference method. The relevant derivatives with their second order (except for the mixed derivative) approximations are

$$\frac{\partial E}{\partial k_x} \approx \frac{E_{i-2} - 8E_{i-1} + 8E_{i+1} - E_{i-2}}{12\Delta x} \quad \text{figure 2.4a} \qquad (2.10)$$

$$\frac{\partial E}{\partial k_y} \approx \frac{E_{j-2} - 8E_{j-1} + 8E_{j+1} - E_{j-2}}{12\Delta y} \quad \text{figure 2.4b} \qquad (2.11)$$

$$\frac{\partial^2 E}{\partial k_x^2} \approx \frac{-E_{i-2} + 16E_{i-1} - 30E_i + 16E_{i+1} - E_{i+2}}{12(\Delta x)^2} \quad \text{figure 2.4c} \qquad (2.12)$$

$$\frac{\partial^2 E}{\partial k_y^2} \approx \frac{-E_{j-2} + 16E_{j-1} - 30E_j + 16E_{j+1} - E_{j+2}}{12(\Delta y)^2} \quad \text{figure 2.4d} \qquad (2.13)$$

$$\frac{\partial^2 E}{\partial k_x \partial k_y} \approx \frac{E_{i+1,j+1} - E_{i+1,j-1} - E_{i-1,j+1} + E_{i-1,j-1}}{4\Delta x \Delta y} \quad \text{figure 2.4e.} \qquad (2.14)$$

The first derivatives are used to calculate the group velocity of the states. The velocity is given by

$$v_\alpha = \hbar^{-1} \frac{\partial E}{\partial k_\alpha}, \qquad (2.15)$$

where $\alpha = x, y$. The second derivatives are required for calculation of the effective mass tensor in the parabolic band approximation:

$$\left[m^{-1}\right]_{\alpha\beta} = \hbar^{-2} \frac{\partial^2 E}{\partial k_\alpha \partial k_\beta}. \qquad (2.16)$$

Note that here a matrix inverse is meant, rather than a scalar reciprocal.

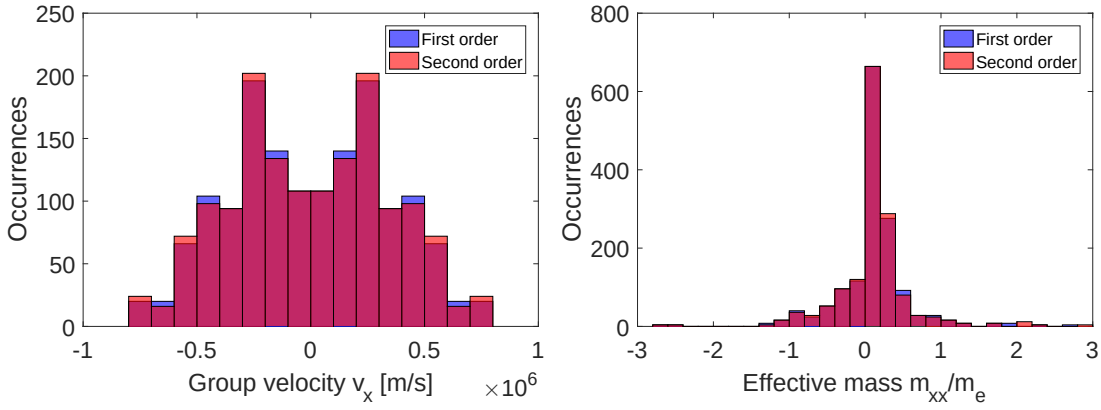

(a) v_x (b) m_{xx}

Figure 2.3.: Distribution of the velocity and effective mass, calculated using both a first and a second order central differences scheme. Derivatives were calculated on the grid from figure 2.4b.

The derivatives were calculated using a first order method as well and then compared on the grid that was used for magnetoresistance calculations. That grid is limited in density, thus using a higher order scheme makes sense. There is a drawback. The derivatives should be taken using energies belonging to the same band. The computer has no notion of bands. For each point in the k_x–k_y plane, it just has an ordered set of eigenvalues. Thus when bands cross exactly where a derivative is taken, it might be that a wrong state is used in the calculation. A first order scheme reduces the chances of this happening because it used only direct neighbors of the state.

In figure 2.4, the value of the derivative in each state is represented by its color. The figure shows slices through three different band structures. The double hexagon resulted from the Schrödinger equation without electrostatics. The other slices result from more realistic Schrödinger-Poisson calculations, that will be used for magnetoresistance calculations later on. The figures reveal the expected symmetry in the first and second order derivatives. One can also see the expectation values for the spin, which are strictly correlated to the wave vector due to strong spin-orbit coupling. The two circles have opposite spin direction.

2.3. Schrödinger-Poisson calculation

After solving the Schrödinger equation, the wave functions of all electrons in the system are known. They will not be spread homogeneously: after all, some electrons will stick to the surfaces. The charge distribution will result in an electrostatic potential in the thin-film. Since the charge distribution is known, the potential can be calculated using Poisson's equation:

$$\nabla^2\phi(\mathbf{r}) = -\frac{\rho(\mathbf{r})}{\epsilon}. \tag{2.17}$$

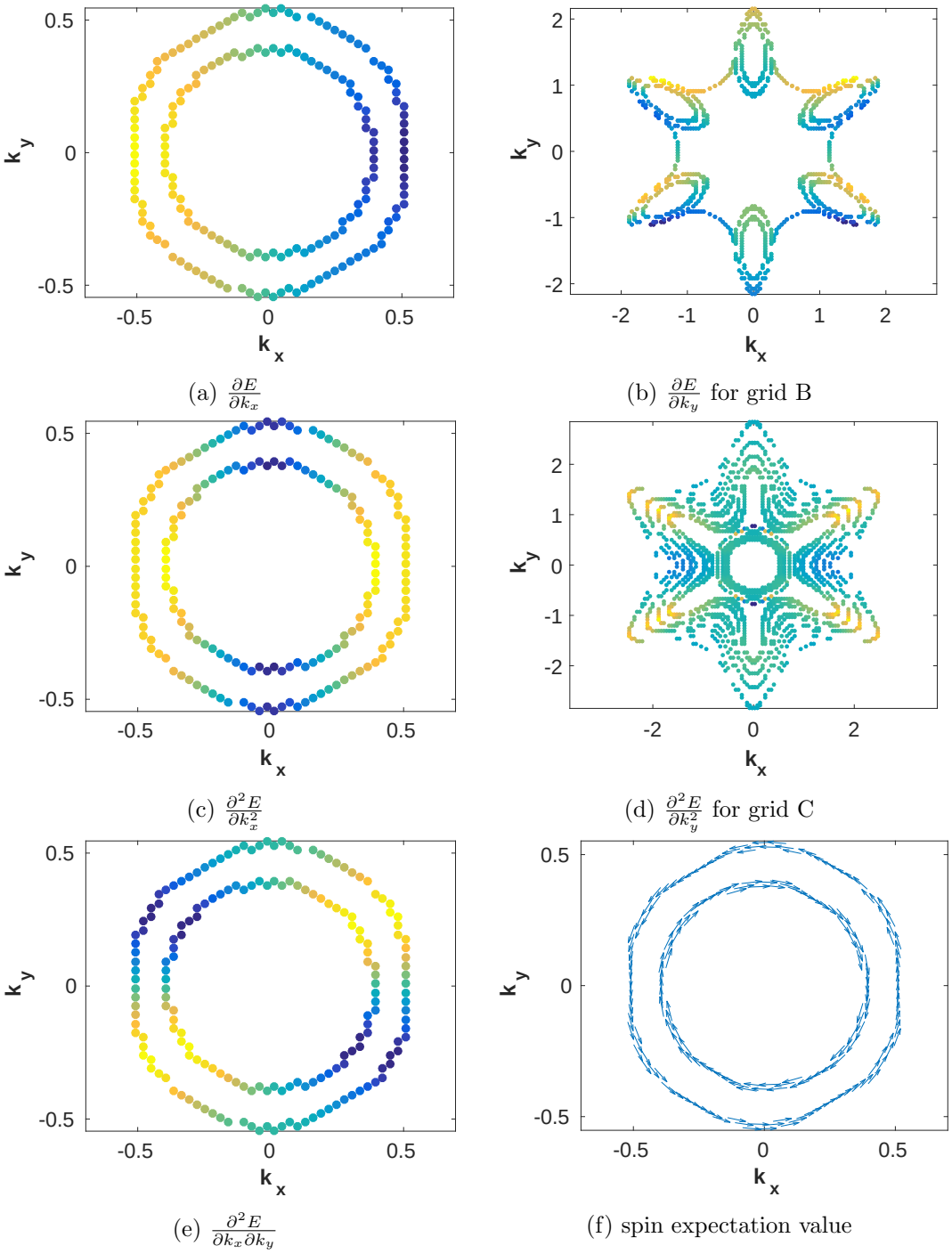

(a) $\frac{\partial E}{\partial k_x}$

(b) $\frac{\partial E}{\partial k_y}$ for grid B

(c) $\frac{\partial^2 E}{\partial k_x^2}$

(d) $\frac{\partial^2 E}{\partial k_y^2}$ for grid C

(e) $\frac{\partial^2 E}{\partial k_x \partial k_y}$

(f) spin expectation value

Figure 2.4.: These figures show all the different derivatives and the expectation values for the spin. Most figures show the $k_x - k_y$ surface for $E = 0$ in figure 2.2. Figures 2.4b and 2.4d demonstrate the surfaces for the last two cases in section 7.1.1 and 7.1.2, respectively.

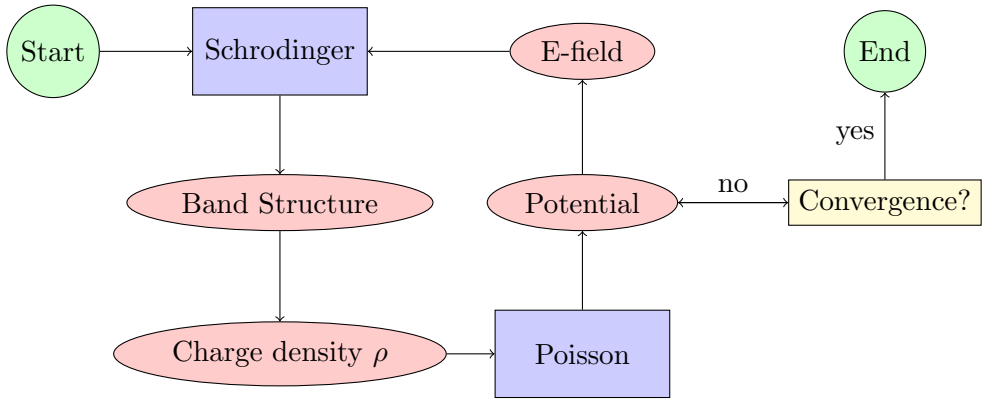

Figure 2.5.: Schematic of the Schrödinger-Poisson solver. Blue boxes represent solvers, red boxes results.

The Poisson equation is a partial differential equation of elliptic type. Here, ρ is the charge density and ϕ the potential. The dielectric constant of Bi_2Te_3 is taken $\epsilon = 218$ based on measurements by Zimmer et al. [12].

The charge distribution is given on the domain $\Omega \subset \mathbb{R}^3$. NEMO5 solves Poisson's equation using a finite element method. The FEM domain is based on the atomistic unit cell. The first two Dirichlet boundary conditions are

$$\phi = v_1 \text{ on } \partial\Omega_1, \qquad \phi = v_2 \text{ on } \partial\Omega_2. \tag{2.18}$$

These are the boundaries of the domain that lie on the surfaces of the thin-film, on which the voltages v_1 and v_2 are applied. The boundary connects through the thin-film, where the FEM solver implements periodic boundary conditions.

In the first iteration of the Schrödinger equation, the electrostatic potential was set to zero to obtain a guess for the wave functions. To obtain the correct band structure it is necessary to solve the Schrödinger and Poisson's equations self-consistently as sketched in figure 2.5. The former provides the band structure, the latter the potential, and both are solved alternately up to some convergence criterium. As boundary conditions, the voltage is set to zero at the surfaces. Two different Schrödinger solvers are used in NEMO5: a low resolution density solver in the self-consistent loop, and a solver with higher accuracy that runs only once after convergence.

Figure 2.6a shows the band structure calculated using the self-consistent Schrödinger-Poisson solver. The dispersion of the Dirac cones is no longer linear as in the Schrödinger calculation, and the Dirac point has shifted down. The double cones now overlap, but there are still four bands involved. The M and K directions still show qualitatively different behavior. The electric potential plot shows a clear maximum in the middle of the film. Note that the chemical potential is obtained by multiplying the electric potential by a factor of -1, due to the negative charge of electrons. A maximum thus indicates that the mobile electrons are redistributed to the surfaces. That makes sense, for that is where the surface states should be.

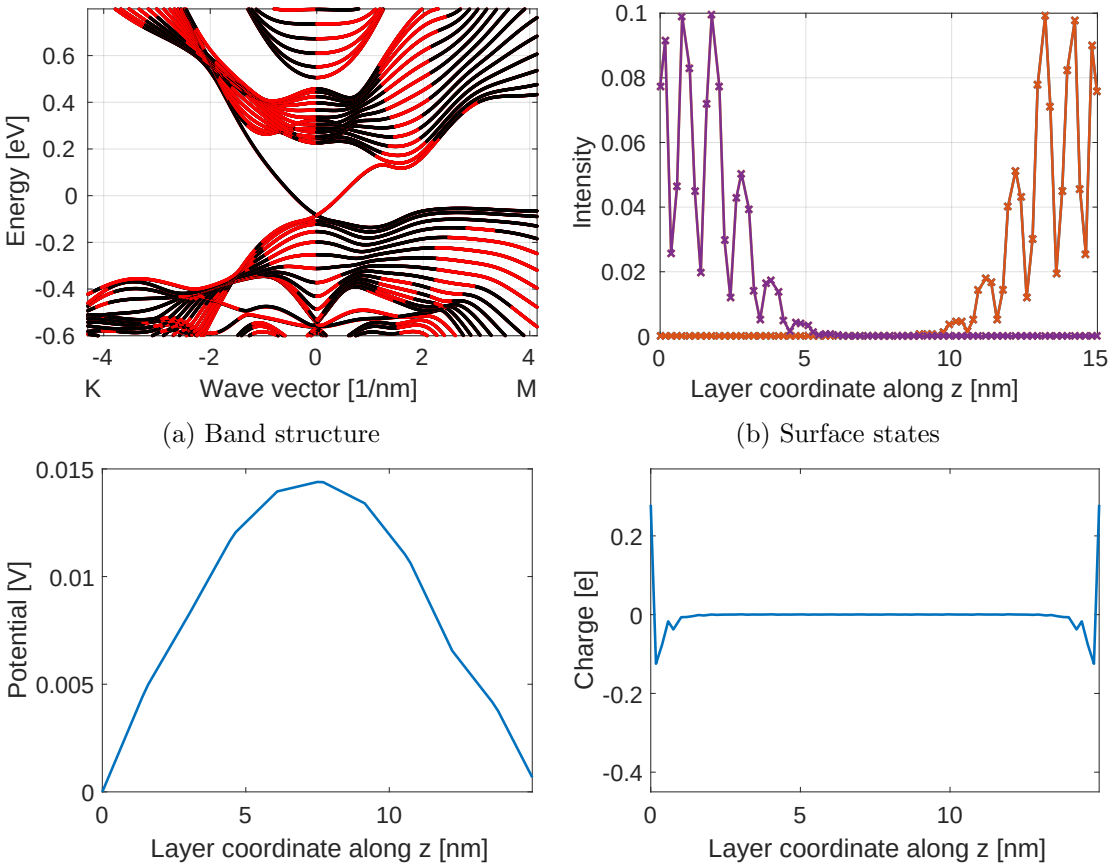

(a) Band structure

(b) Surface states

(c) Potential landscape

(d) Free charge distribution

Figure 2.6.: Self-consistent Schrödinger-Poisson calculation.

2.3.1. Surface states

A simple verification of the Schrödinger-Poisson solver is to plot the wave function for some state in the Dirac cone. The wave functions should still be clearly bound to one of the two surfaces. Figure 2.6b shows the wave functions for the four states in the Dirac point. Only two functions can be seen, as each surface has two states with opposite spin with overlapping wave functions in real space.

3. Validation

The band structure will first be compared to verified calculations using NEMO5, to make sure it works correctly. After that, the convergence is investigated for the Schrödinger-Poisson calculation. Lastly, the band structure is compared with experimental results.

3.1. Comparison with sample problems

3.1.1. Schrödinger

NEMO5 comes bundled with a number of reference systems and the corresponding results to verify the installation of the software. One of these tests calculates the band structure of a 9 QL Bi_2Te_3 film without taking any potential in consideration. This simple Schrödinger calculation itself is not interesting, but it was used to validate the installation because of its similarities to the simulations for the project.

The reference data consists of 60 points in k-space, for each of which there are 900 eigenvalues. It is thus a 60×900 matrix with entries $E_{n,k}$. Define the locally calculated eigenvalues as $\hat{E}_{n,k}$. The relative matrix error is then given by

$$\frac{||\hat{E} - E||_2}{||E||_2} = 4.878 \cdot 10^{-14}. \tag{3.1}$$

Since for each point in k-space an independent eigenvalue problem is solved, it makes sense to also look at the error per k-point. The relative error in the vectors is

$$\frac{||\hat{E_k} - E_k||_2}{||E_k||_2}. \tag{3.2}$$

This error is shown in figure 3.1. Symmetry around the y-axis is expected since the band structure itself is, for these paths in k-space, symmetric around it as well. Although the peaks are remarkable, one can safely conclude that the sets of eigenvalues approximate the reference data up to 13 decimal digits.

3.1.2. Schrödinger-Poisson

Another test with reference data is available for a Schrödinger-Poisson calculation on the same system as in the previous chapter. The data comes in the form of the potential along the z-axis. When comparing to the local calculations, no error was observed at all, indicating that the FEM solver works as it should.

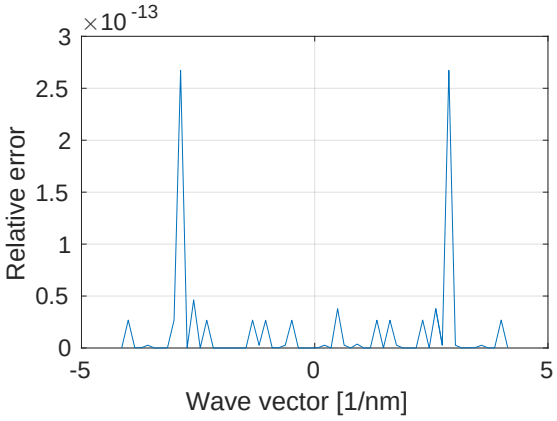

Figure 3.1.: Relative error in the 2-norm per point in k-space

3.2. Convergence and accuracy

The Schrödinger-Poisson solver functions properly, but it is necessary to determine which precision should be used. A criterion on the L_2 norm of the difference in potential is used to determine if the self consistent loop has converged. It is set to a precision of six decimals (in Volts) by default, and this was not changed. Two other factors are important here:

k-space sampling density, which sets the number of k-points that are used in the Schrödinger solver each iteration. Note that this is *not* the high-resolution solver that runs only once *after* convergence of the self consistent loop. A higher resolution in k-space gives a more accurate picture of where the wave functions are located. In other words, it hands a more precise charge distribution to the Poisson solver.

FEM mesh density, which influences the level of detail in the obtained potential landscape. The FEM mesh is built up from the atomistic grid. NEMO5 gives the option to refine this mesh, which is done by placing an extra node between all existing nodes.

The density of the k-space sampling is set by a scalar option k_{dens}. This scalar sets the number of steps along the x, y and z axis, meaning that the actual number of k-points equals k_{dens}^3. In figure 3.3, k_{dens} was varied from 10 to 40. Based on the error shown in figure 3.2 it was decided to use $k_{dens} = 20$ for following calculations.

The FEM mesh is more troublesome. When refining the mesh more than once, the Poisson solver suddenly converges to a potential which is orders of magnitude larger and clearly non-physical. It is likely caused by the way the mesh is created from the atomistic grid. The difference between no refinement and refining once is clearly visible. Even though the energy shift is small, it causes the degenerate bands to separate a little more. This is clearly seen from the coloring of the bands, which seems more consistent.

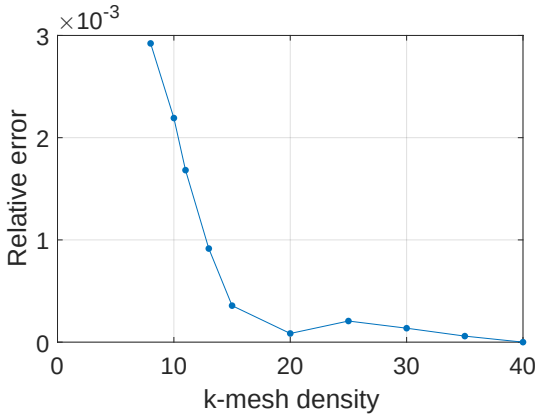

Figure 3.2.: Relative error of the total band structure in the 2-norm

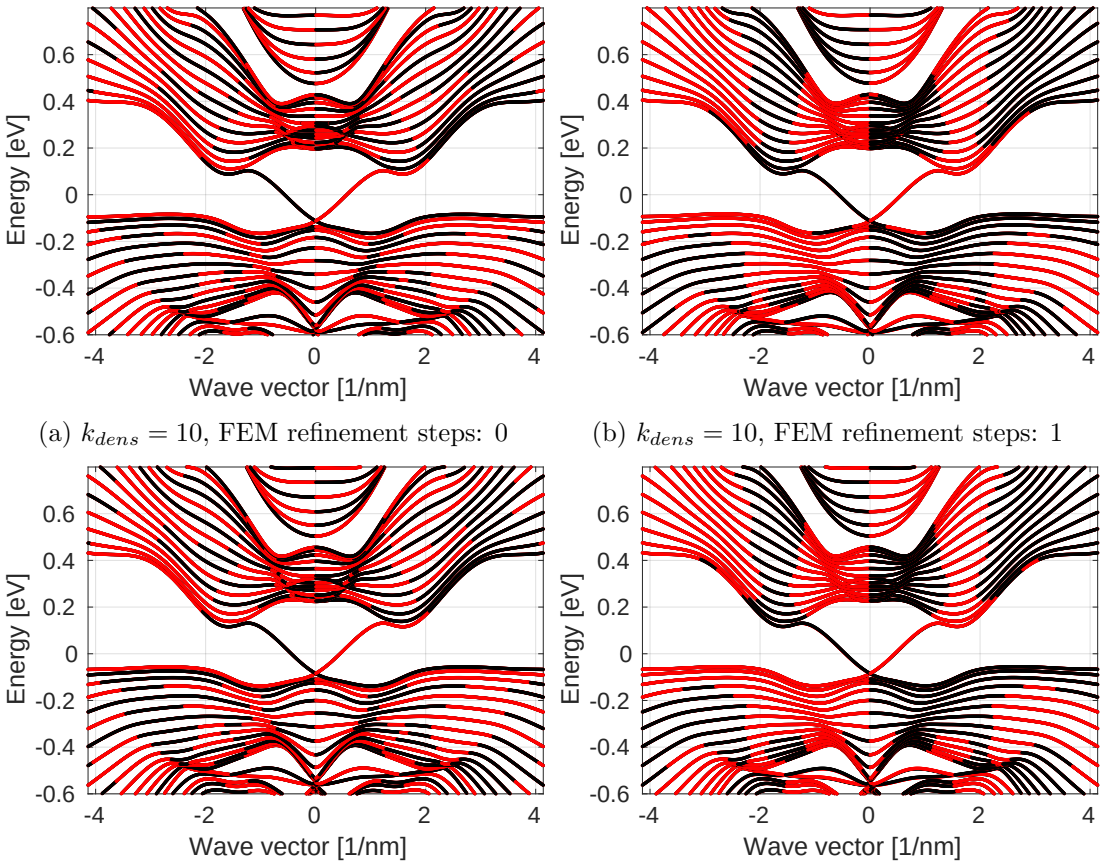

(a) $k_{dens} = 10$, FEM refinement steps: 0

(b) $k_{dens} = 10$, FEM refinement steps: 1

(c) $k_{dens} = 40$, FEM refinement steps: 0

(d) $k_{dens} = 40$, FEM refinement steps: 1

Figure 3.3.: Convergence plots, along the M-Γ-M path

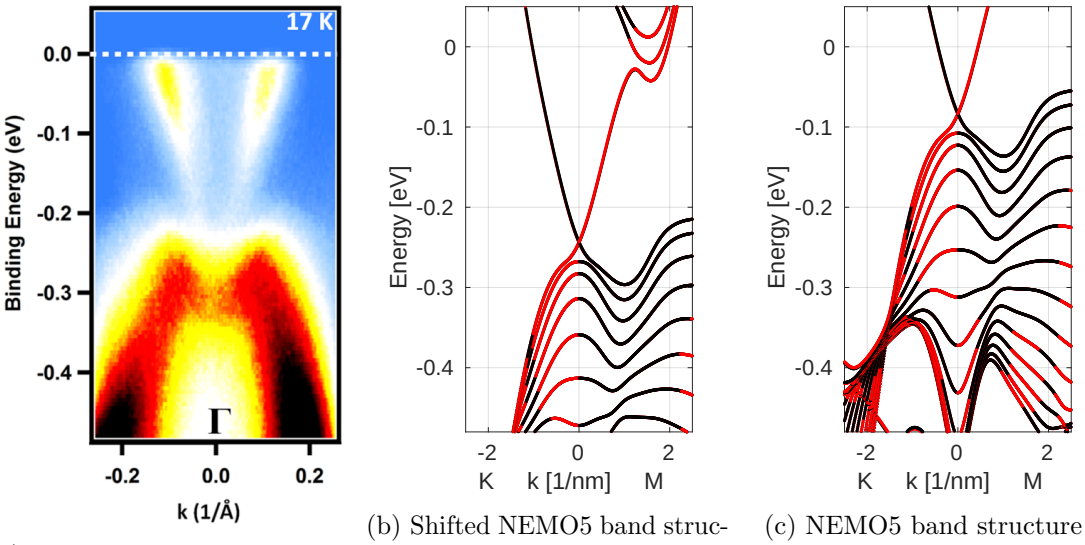

(a) ARPES measurement by Ngabonziza et al. [13]

(b) Shifted NEMO5 band structure

(c) NEMO5 band structure

Figure 3.4.: Comparison with ARPES.

3.3. Comparison with experiment

The calculated band structure is compared with experimental results. These are obtained trough angle-resolved photoemission spectroscopy, or ARPES. A beam of photons is directed at the sample. Electrons can absorb these photons and escape, which is known as the photoelectric effect. The kinetic energy that they carry is related to the difference between the energy of the incoming electrons and the binding energy. The angle at which electrons escape reveals their momentum prior to absorption of the photon.

Figure 3.4 compares the calculated band structure with ARPES measurements. Those experiments were performed for a 15 QL thin-film, just like the calculations. A difference is the substrate of SrTiO, which is not included in the model. The rightmost figure is calculated by NEMO5. The middle figure is the same band structure, shifted to match the energy of the Dirac point with that of the experiment. The experiment was likely performed in the M direction, but this was not documented. The calculations produce an M-shape in the bulk valence band around the Dirac point. However, it is wider than in the ARPES figure. For $|\mathbf{k}| \geq 2\,\mathrm{nm}^{-1}$, the bands disappear in ARPES but are visible in the calculated band structure. The wave function in figure 3.5 is from the same band as the Dirac cone. It reveals that the surface states are further in the bulk for larger wave vectors. It might be that the ARPES cannot detect these electrons.

This image reveals that the Fermi level of the experiment comes close to some bulk conduction bands. This supports the idea that bulk conduction bands could contribute to transport. The Fermi level raises further towards the bulk bands after exposure to air, due to adsorbates collecting on the surface.

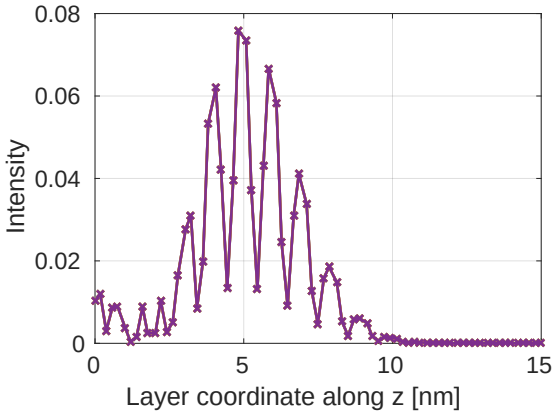

Figure 3.5.: A surface state wave function for $|\mathbf{k}| = 2.14\,\mathrm{nm}^{-1}$.

4. Results for physical scenarios

This chapter will present various results of calculations made with NEMO5. The aim is to simulate physically relevant scenarios. Some of these scenarios will be used for magnetoresistance calculations in chapter 7.

This thesis focuses on a thin-film that consists of 15 QL. In the first scenario, the thickness is reduced even further. It is expected that the topological surface states will break down, due to hybridization, in the ultra-thin-film limit.

The second scenario will try to simulate a thin-film that has been exposed to air or chemicals. Such exposure leads to surface doping by adsorbates. This process will be mimicked by adjusting the electrostatic boundary conditions in the FEM solver.

In the third scenario, an external magnetic field will be applied on the thin-film. First, the implementation in the tight-binding method is discussed. Next, the effect of the magnetic field on the spin expectation value in the bulk and surface bands is studied. The Zeeman effect turns out to be much weaker than expected.

4.1. Ultra-thin-films

For ultra-thin-films, the Dirac cone will open so that a gap is observed in the band structure [14, 15]. Here, it is investigated if the tight-binding model can replicate this phenomenon. One way to understand gapping of the surface states for ultra-thin-film Bi_2Te_3 is by picturing their wave functions. As the film gets thinner, the electrons that were confined at the surfaces start interact with one another. Their wave functions begin to overlap and hybridize, increasing their energy. This means that no true surface states exist anymore and the material is no longer a topological insulator. In figure 4.1, the previous surface state wave functions and band structure can be seen for a sample of 6 QL. A gap has opened in the Dirac cone. Due to the unit cell formed by 3 QL in NEMO5, not any thickness can be simulated. For 3 QL, a gap opens as well. For 9, 12 and for 15 QL, the Dirac cone is not gapped.

4.2. Electrostatic boundary conditions

When a thin-film sample is exposed to air, adsorbates and contaminants collect on the surface. The same happens when the sample comes in contact with chemicals during its fabrication. Such pollutants can be charged. These extra surface charges cause an (unwanted) potential near the thin-film surface. The resulting electric field is screened in the bulk of the material, so that the electrons near the surface feel a larger shift

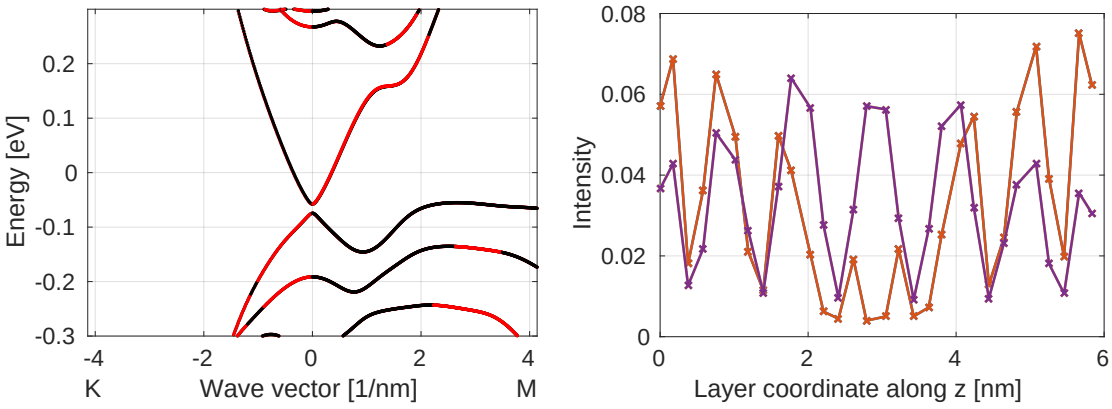

(a) Band structure (b) Surface states

Figure 4.1.: Schrödinger-Poisson calculation for 6 QL.

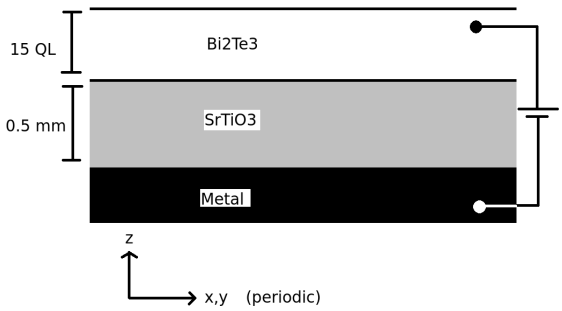

Figure 4.2.: Schematic of the Bi_2Te_3 system with back gating

in chemical potential than those further in the bulk. Bands are shifted in energy as a function of their position in the material. This effect is called *band bending*.

Band bending can also be caused by electrostatic gating. The thin-films are grown on a dielectric substrate. In the case of back gating, a voltage difference is applied between the thin-film and the backside of the substrate, as shown in figure 4.2. The voltage difference induces an electric field near the bottom surface of the substrate. The field is screened in the thin-film, and this results in band bending.

Both effects are simulated by applying nonzero electrostatic potentials to the surfaces. The electrochemical potential is not changed from previous calculations. Figure 4.3 shows band structures and potentials for substrates with the bottom surface potential fixed at 0 V and the top surface potential set to $\pm$ 0.5 V. Electrons have a negative charge, and are thus attracted to regions with a positive potential. The asymmetry of both potential landscapes is striking. The negative voltage is quickly screened by depletion of electrons in that region, while this is not the case for the positive voltage.

In the sample with a negative potential applied, electrons are forced away from the top surface. For electrons that are still near the top surface, the chemical potential is increased considerably. One of the Dirac cones is shifted upwards in the band structure

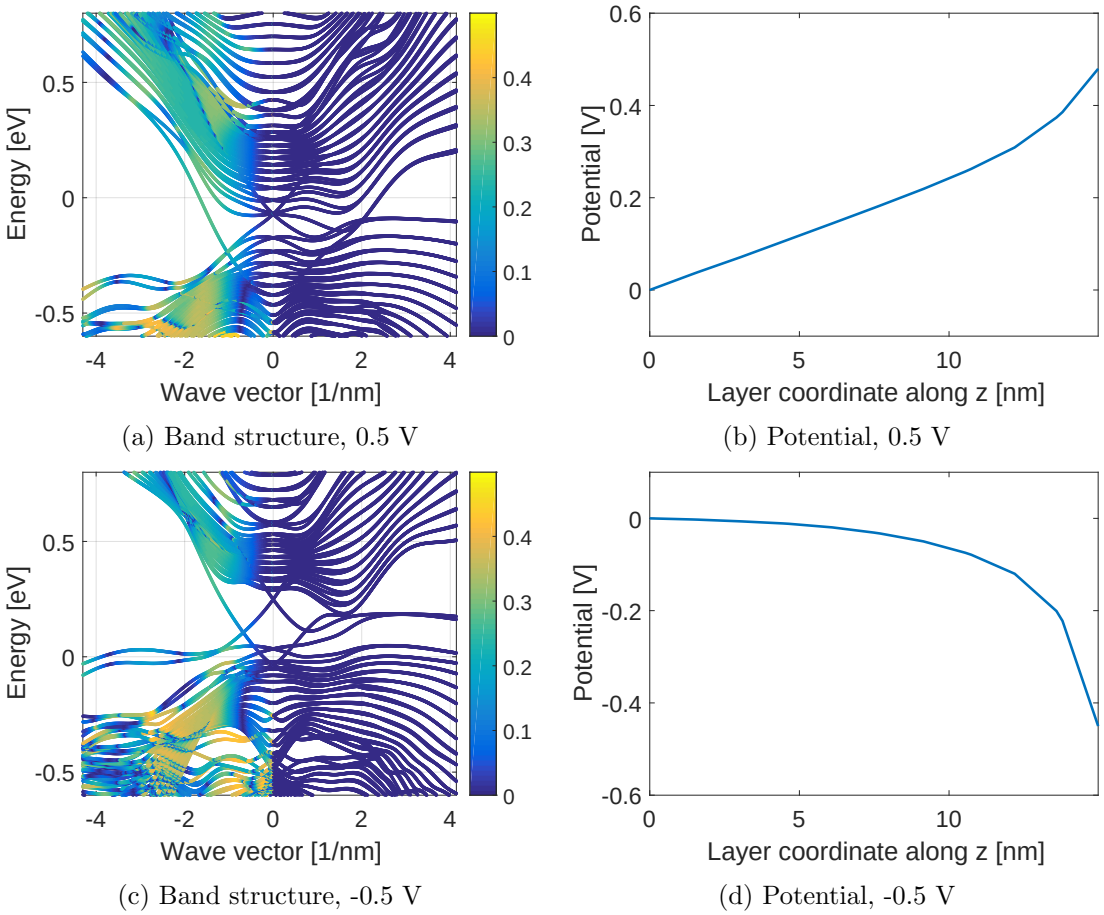

(a) Band structure, 0.5 V

(b) Potential, 0.5 V

(c) Band structure, -0.5 V

(d) Potential, -0.5 V

Figure 4.3.: Band splitting for different surface potentials.

as a result. Most of the states in the bulk and near the bottom surface have only a slight increase in chemical potential. This if reflected by a minor shift for other bands in the band structure.

The positive potential causes a negative shift in the chemical potential of electrons, that is almost linear along the thin-film. Compared to the previous case, a larger portion of the bulk bands is significantly shifted.

4.3. Magnetic field

4.3.1. Tight-binding model

A magnetic field will have an influence on the band structure of a material. To account for these effects, it is necessary to make adjustments to the Hamiltonian. NEMO5 has options for making two of these adjustments to the tight-binding model. They can be turned on an off separately, but will always be used together.

Peierls subsitution

The first adjustment is the Peierls substitution. It describes the effect of a magnetic field on the orbit of an electron. The Peierls substitution is an approximation, suitable for a slowly varying vector potential $\boldsymbol{A}(\boldsymbol{r}, t)$. The substitution is usually described in second quantization.

In second quantization, the tight-binding parameters α, β, γ are replaced with hopping parameters t. They describe how electrons hop in different directions in the material. The Peierls substitution adds the *Peierls phase* to the hopping parameters:

$$t_{ij} \rightarrow t_{ij} e^{i\frac{e}{\hbar}\int_i^j \boldsymbol{A}\cdot d\boldsymbol{l}}. \tag{4.1}$$

Here, $\int_i^j \boldsymbol{A} \cdot d\boldsymbol{l}$ is the line integral of the vector potential along the hopping path.

Zeeman splitting

The Peierls substitution describes the effect of the magnetic field on the orbit of the electrons. Another term is necessary for the effect of the field on the spin. Unfortunately, the exact implementation of the Zeeman splitting in NEMO5 is not known.

4.3.2. Spin alignment

In absence of a magnetic field, the spin-orbit coupling in Bi_2Te_3 causes perpendicular spin-momentum locking. It is interesting to see how a magnetic field breaks this locking, because this is believed to be a mechanism for magnetoresistance[10]. Figure 4.4 shows the band structure diagram for a thin-film, with and without a perpendicular magnetic field. The color indicates the absolute value of the spin-z component. For zero magnetic field, the spin-z component is relatively small. In the right part of the plot, the states have no spin-z component because it runs in a specific (M) direction. Along this line in the Fermi surface, the spin-z component happens to change sign. The fact that the z-components are all zero is convenient when comparing with the case with a magnetic field. When a magnetic field is applied, almost all states align their spin with (or against) the field. An important exception is the Dirac cone. It seems that the spin of a topological surface state is very robust against a magnetic field.

This difference in spin alignment indicates that the spin-orbit interaction is not constant through the thin-film. More precisely, the topological surface states have stronger spin-momentum locking than the states in the bulk.

The theory from section 1.4 relates magnetoresistance to spin alignment under influence of a magnetic field. Based on the observations, no positive magnetoresistance should occur if only the topological surface states contribute to the transport. When the lowest bulk conduction bands are involved as well, positive magnetoresistance can be expected.

4.3.3. Band shift

In presence of a magnetic field, a magnetic dipole will feel a shift in potential energy. This energy depends on the angle between the magnetic field and the magnetic moment

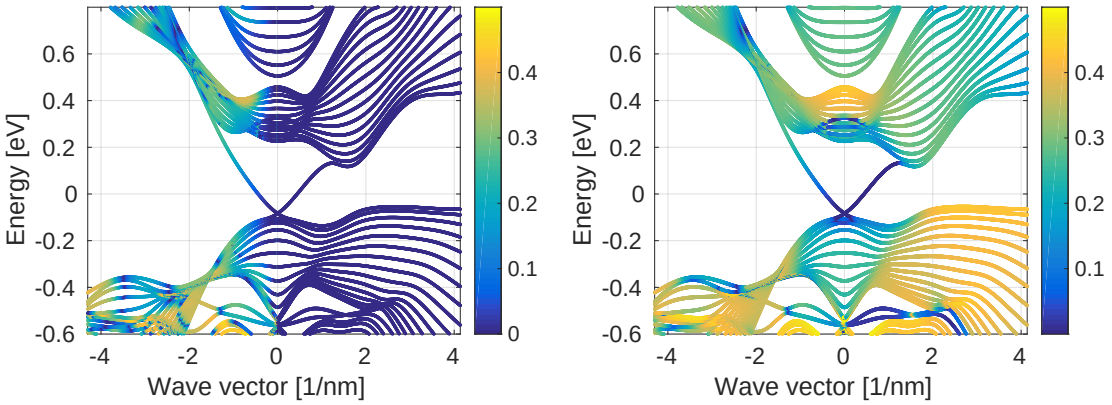

(a) B = 0 T (b) B = 20 T

Figure 4.4.: Spin-z expectation value

	B = 0	B = 20	B = 60	B = 200	g-factor
Surface	0	0.29	0.85	2.82	0.24
Bulk	0	1.4	4.4	13.8	1.08

Table 4.1.: Energy gaps in meV for surface and bulk states.

of the dipole. In the band structure of Bi_2Te_3, all bands are double degenerate for spin up and down. When applying a magnetic field, the bands will therefore shift in opposite directions. The splitting of bands is called Zeeman splitting.

The energy shift in the band structure is described by

$$\Delta E = \frac{1}{2} g_{\text{eff}} \mu_{\text{B}} B, \tag{4.2}$$

for effective g-factor g_{eff} and Bohr magneton μ_B. The effective g-factor is different for different bands in the band structure. To calculate it, energy shifts were measured at the gamma point. This was done for the Dirac cone (see figure 4.5) and a bulk band at ±500 meV. The energy shifts were obtained by measuring the energy difference between two bands and dividing this by a factor of two, to account for the fact that both bands shift simultaneously.

The results are gathered in 4.1. It shows the energy distance between states had exactly the same energy when no magnetic field was applied. An approximation of the effective g-factor was calculated by a linear fit.

4.4. Discussion

The effective g-factor is calculated for a surface and for a bulk band at the gamma point. A significant discrepancy exists between the calculated effective g-factor and those

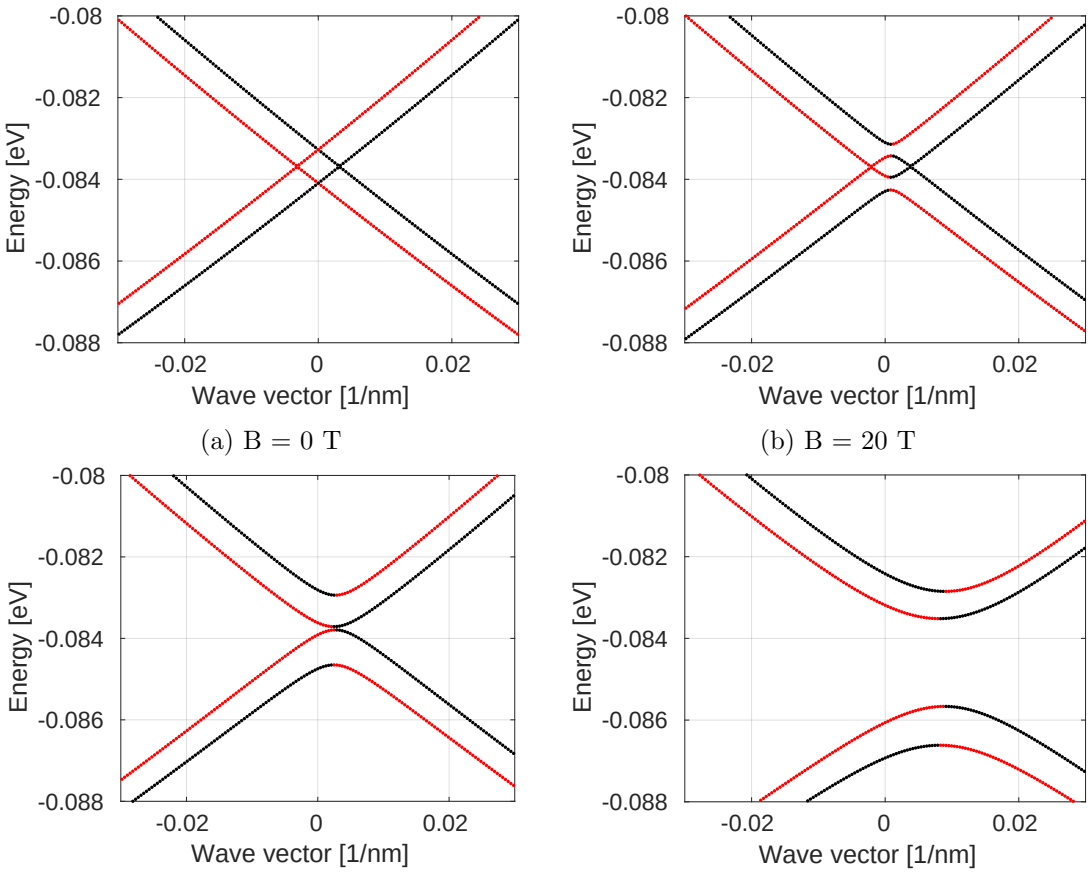

(a) B = 0 T

(b) B = 20 T

(c) B = 60 T

(d) B = 200 T

Figure 4.5.: Band splitting for various magnetic fields.

observed in literature, which are as large as 20[16, 17]. The band shifts were much smaller than expected.

It is unlikely that the discrepancy is caused by the Peierls substitution. It has been implemented in NEMO5 for a long time and was thoroughly tested. However, the effect of the magnetic field on the spin is clearly observed. That is an indication that at least a part of the Zeeman term works correctly. The unexplained behavior in a magnetic field must be kept in mind when interpreting the results of the magnetoresistance calculations. Until this issue is resolved, it makes only sense to do qualitative predictions.

Part II.

Magnetoresistance

5. Theory

The next objective is to calculate the resistivity of the thin-film as a function of a perpendicular magnetic field. To this end, the conductivity will be calculated using the Boltzmann model. Various results of the Schrödinger-Poisson calculations are required to obtain the conductivity. This chapter will discuss the relevant theory, including the Boltzmann model, the linearized Boltzmann equation, and the relaxation time approximation. Consulted literature for this chapter is Ashcroft and Mermin [5, Chapters 13, 16].

The conductivity will be calculated using the Boltzmann model. The simpler Drude model makes the assumption of isotropic bands, which is not true for the Bi_2Te_3 system. The energy of an isotropic band depends only on the magnitude of the wave vector, not on the direction. With the Boltzmann model, this assumption will still be made implicitly through the relaxation time approximation. An improvement over the Drude model is that the relaxation time can depend on the wave vector.

First, the distribution function is defined as

$$f_n(\mathbf{r}, \mathbf{k}, t) \frac{d^3 r d^3 k}{(2\pi)^3}, \tag{5.1}$$

which equals the number of electrons in band n at time t within the phase space volume $d^3r\, d^3k$ around the point $\mathbf{r}$, $\mathbf{k}$. The current density is given by

$$\mathbf{j} = -e \sum_n \int_{\mathrm{BZ}} f_n(\mathbf{r}, \mathbf{k}, t) \mathbf{v}_n(\mathbf{k}) \frac{d^3 k}{(2\pi)^3}, \tag{5.2}$$

for bands n, group velocity v_n and distribution function $f_n(\mathbf{r}, \mathbf{k}, t)$. Summing over the bands will not be done explicitly in the implementation. The integral will be evaluated for all states, irrespective of their band.

The group velocities can be calculated directly from the band structure as follows:

$$\boldsymbol{v} = \hbar^{-1} \frac{\partial E}{\partial \mathbf{k}^T}. \tag{5.3}$$

It is necessary to find and expression for the distribution function. The Fermi-Dirac distribution is defined as

$$f^0(\mathbf{k}) = \left(e^{\frac{E(\boldsymbol{k}) - \mu}{k_{\mathrm{B}} T}} + 1 \right)^{-1}, \tag{5.4}$$

where k_{B} is Boltzmann's constant, T is the temperature and μ the chemical potential. The distribution is written as the sum of the Fermi-Dirac distribution f^0 and a deviation δf

$$f(\mathbf{r}, \mathbf{k}, t) = f^0(\mathbf{k}) + \delta f(\mathbf{r}, \mathbf{k}, t). \tag{5.5}$$

These functions will be written as a function of the wave vector for clarity.

When inserted in equation 5.2, the Fermi-Dirac distribution will not contribute to the conductivity, because it describes the occupation of states in equilibrium. It is therefore only necessary to calculate the deviation. This deviation is described by the linearized Boltzmann equation (LBE), which reads

$$\frac{\partial \delta f(\mathbf{k})}{\partial t} - \frac{e}{\hbar}\boldsymbol{v} \times \mathbf{B} \cdot \frac{\partial \delta f(\mathbf{k})}{\partial \mathbf{k}} + \boldsymbol{v} \cdot \left[e\boldsymbol{\mathcal{E}} + \frac{E-\mu}{T}\nabla T \right] \left(-\frac{\partial f^0(\mathbf{k})}{\partial E} \right) = \mathcal{T}(f(\boldsymbol{k})). \tag{5.6}$$

For a static electric field, the distribution function is not a function of time, so that the time derivative becomes zero. $\mathcal{T}$ is the collision integral. A general expression is given by

$$\mathcal{T} = -\int \frac{d^3k}{(2\pi)^3} \left(W_{\boldsymbol{k},\boldsymbol{k'}} f(\boldsymbol{k})[1 - f(\boldsymbol{k'})] - W_{\boldsymbol{k'},\boldsymbol{k'}} f(\boldsymbol{k'})[1 - f(\boldsymbol{k})] \right). \tag{5.7}$$

$W_{\boldsymbol{k},\boldsymbol{k'}}$ is defined using the scattering probability. The probability that an electron with wave vector $\boldsymbol{k}$ scatters to a state with wave vector contained in d$\boldsymbol{k'}$ around $\boldsymbol{k'}$, in the time interval dt, assuming that the state is unoccupied, is given by

$$\frac{W_{\boldsymbol{k},\boldsymbol{k'}} dt d\boldsymbol{k'}}{(2\pi)^3}. \tag{5.8}$$

The scattering is assumed to be elastic. This means that electrons can only scatter to states with the same energy. Furthermore, it is assumed that the impurities which cause scattering are dilute enough. Then it can be shown that

$$W_{\boldsymbol{k},\boldsymbol{k'}} = \frac{2\pi}{\hbar} n_{\text{imp}} |\left\langle \boldsymbol{\psi(k')} \right| U \left| \boldsymbol{\psi(k)} \right\rangle|^2 \delta(E_{\mathbf{k}} - E_{\mathbf{k}'}) = W_{\boldsymbol{k'},\boldsymbol{k}}. \tag{5.9}$$

The impurity density, n_{imp}, is the number of scatterers per unit volume. U describes the interaction between an electron and an impurity. The symmetry in W follows from the fact that U is Hermitian. With this symmetry, equation 5.7 for the collision integral can be simplified to

$$\mathcal{T} = -\int \frac{d^3k}{(2\pi)^3} W_{\boldsymbol{k},\boldsymbol{k'}} [f(\boldsymbol{k}) - f(\boldsymbol{k'})]. \tag{5.10}$$

5.1. Relaxation time approximation

It is not possible to solve the LBE with expression 5.10 for the collision integral analytically. Therefore, the relaxation time approximation (RTA) is used. In the RTA, the collision integral is written as

$$\mathcal{T} = -\frac{\delta f(\boldsymbol{k})}{\tau(\boldsymbol{k})}. \tag{5.11}$$

Where the relaxation time $\tau(\boldsymbol{k})$ does *not* depend on the distribution function. While this simplifies the collision integral, it is still necessary to find an expression for the scattering time τ.

For very specific cases, solving the LBE with the RTA gives the same result as solving the LBE without the RTA. The material must have isotropic bands and isotropic elastic impurity scattering. Thus, the energy must depend only on the magnitude k of the wave vector. The scattering probability between two states must depend only on the common value of their energy, and on the angle between their wave vectors. Furthermore, the electric field must be spatially uniform and static. Note that these requirements are not met in the Bi_2Te_3 system. Applying the RTA will, therefore, have an influence on the calculated conductivity.

By comparing the two cases, an expression for the relaxation time can be found. Demand that

$$\int \frac{d^3k}{(2\pi)^3} W_{\boldsymbol{k},\boldsymbol{k'}} \left([f(\boldsymbol{k}) - f(\boldsymbol{k'})] \right) = \frac{\delta f(\boldsymbol{k})}{\tau(\boldsymbol{k})}. \tag{5.12}$$

In the RTA, for a system that meets all the described requirements, the distribution function is of the form

$$f(\mathbf{k}) = f(\mathbf{k})^0 + \mathbf{k} \cdot \mathbf{A}(E). \tag{5.13}$$

The vector function $A(E)$ depends on k only through its magnitude, i.e., only through E. Since $W_{\boldsymbol{k},\boldsymbol{k'}}$ is only nonzero for $E(\boldsymbol{k}) = E(\boldsymbol{k'})$, this reduces equation 5.12 to

$$\mathbf{A}(E) \cdot \int \frac{d^3k}{(2\pi)^3} W_{\boldsymbol{k},\boldsymbol{k'}}(\boldsymbol{k} - \boldsymbol{k'}) = \frac{1}{\tau(\boldsymbol{k})} \mathbf{k} \cdot \mathbf{A}(E). \tag{5.14}$$

Now, rewrite the vector $\mathbf{k}'$ as a sum of its components parallel and perpendicular to $\mathbf{k}$

$$\mathbf{k}' = (\hat{\mathbf{k}} \cdot \mathbf{k}')\hat{\mathbf{k}} + \mathbf{k}'_{\perp}. \tag{5.15}$$

The scattering is isotropic, so $W_{\boldsymbol{k},\boldsymbol{k'}}$ must not depend on $\mathbf{k}'_{\perp}$. For $W_{\boldsymbol{k},\boldsymbol{k'}}$ to be nonzero, the two involved energies must be the same, since elastic scattering was assumed. For isotropic bands, this means that the two involved wave vectors must have the same magnitude, so that $(\hat{\mathbf{k}} \cdot \mathbf{k}')\hat{\mathbf{k}} = (\hat{\mathbf{k}} \cdot \hat{\mathbf{k}}')\mathbf{k}$. Now it is possible to write

$$W_{\boldsymbol{k},\boldsymbol{k'}}\mathbf{k}' = \mathbf{k} W_{\boldsymbol{k},\boldsymbol{k'}}(\hat{\mathbf{k}} \cdot \hat{\mathbf{k}}'). \tag{5.16}$$

Again, a limitation of the RTA appears. When an electron scatters to another band, the two involved states can have the same energy but wave vectors with different magnitudes.

Insertion in equation 5.14 gives the relaxation time

$$\int \frac{d^3k}{(2\pi)^3} W_{\boldsymbol{k},\boldsymbol{k'}}(1 - \hat{\boldsymbol{k}} \cdot \hat{\boldsymbol{k'}}) = \frac{1}{\tau(\boldsymbol{k})}. \tag{5.17}$$

The exact form of $W_{\boldsymbol{k},\boldsymbol{k'}}$ depends on the scattering mechanism. A two dimensional Coulomb potential with Thomas-Fermi screening[5, Chapter 17] is used, given by

$$U = \frac{e^2}{2\epsilon_0\epsilon_r} \frac{1}{(|\mathbf{k} - \mathbf{k}'| + \xi^{-1})}. \tag{5.18}$$

It is inversely proportional to the sum of the magnitude of the difference in wave vectors and inverse of the the Thomas-Fermi screening length ξ.

The final expression for the relaxation time is given by

$$\tau^{-1}(\mathbf{k}) = \int \frac{d^3k}{(2\pi)^3}\frac{2\pi}{\hbar} n_{\text{imp}} \left(\frac{e^2}{2\epsilon_0\epsilon_r}\right)^2 |\left\langle \boldsymbol{\psi(k')}\middle|\boldsymbol{\psi(k)}\right\rangle|^2 \frac{(1-\hat{\mathbf{k}}\cdot\hat{\mathbf{k}}')}{(|\mathbf{k}-\mathbf{k}'|+\xi^{-1})^2}\delta(E_{\mathbf{k}}-E_{\mathbf{k}'}). \tag{5.19}$$

The relaxation time is related to the probability that a certain state scatters to any other state, expressed by the overlap integral of the wave functions ψ. These overlaps will change with the magnetic field. The δ term ensures elastic scattering: particles only scatter to states with the same energy. The term $(1-\hat{\mathbf{k}}\cdot\hat{\mathbf{k}}')$ is a result of the RTA. It ensures that scattering to a state that travels in the same direction as the incoming electron does not influence the conductivity.

5.2. Conductivity

With the expression for the relaxation time, it is possible to solve the LBE. Assume that the system is in a steady state, so that the derivative with respect to time vanishes. The temperature is assumed to be constant, so that the temperature gradient disappears as well. The LBE then becomes

$$e\boldsymbol{v}\cdot\boldsymbol{\mathcal{E}}\frac{\partial f^0}{\partial E} + \frac{e}{\hbar c}\boldsymbol{v}\times\mathbf{B}\cdot\frac{\partial \delta f}{\partial \mathbf{k}} = \frac{\delta f}{\tau}. \tag{5.20}$$

Or, in tensor notation:

$$ev^\alpha \mathcal{E}_\alpha \frac{\partial f^0}{\partial E} + \frac{e}{\hbar}\epsilon_{\alpha\beta\gamma}v^\alpha B^\beta \frac{\partial \delta f(\mathbf{k})}{\partial k^\gamma} = \frac{\delta f(\mathbf{k})}{\tau}. \tag{5.21}$$

The density function was already assumed to be of the form $\delta f(\mathbf{k}) = \mathbf{k}\cdot\mathbf{A}(E)$. This specific form can be used to simplify the term with the magnetic field in the LBE:

$$\begin{aligned}
\epsilon_{\alpha\beta\gamma}v^\alpha B^\beta \frac{\partial \delta f(\mathbf{k})}{\partial k^\gamma} &= \epsilon_{\alpha\beta\gamma}v^\alpha B^\beta \frac{\partial k^\mu A^\mu(E)}{\partial k^\gamma} && (5.22)\\
&= \epsilon_{\alpha\beta\gamma}v^\alpha B^\beta \left(A^\gamma + k^\mu \frac{\partial A^\mu(E)}{\partial k^\gamma}\right) && (5.23)\\
&= \epsilon_{\alpha\beta\gamma}v^\alpha B^\beta \left(A^\gamma + k^\mu \frac{\partial A^\mu(E)}{\partial \epsilon}\frac{\partial E}{\partial k^\gamma}\right) && (5.24)\\
&= \epsilon_{\alpha\beta\gamma}v^\alpha B^\beta \left(A^\gamma + \hbar k^\mu v^\gamma \frac{\partial A^\mu(E)}{\partial E}\right) && (5.25)\\
&= \epsilon_{\alpha\beta\gamma}v^\alpha B^\beta A^\gamma. && (5.26)
\end{aligned}$$

In the last step, it was used that $\epsilon_{\alpha\beta\gamma}v^\alpha v^\gamma = 0$, due to the asymmetry of the Levi-Civita tensor. The LBE becomes

$$ev^\alpha \mathcal{E}_\alpha \frac{\partial f^0}{\partial E} + \frac{e}{\hbar}\epsilon_{\alpha\beta\gamma}v^\alpha B^\gamma A^\beta = \frac{k^\beta A^\beta(E)}{\tau}. \tag{5.27}$$

The effective mass is defined proportional to the Hessian of the energy:

$$\left[m^{-1}\right]_{\alpha\beta} = \hbar^{-2}\frac{\partial^2 E}{\partial k_\alpha \partial k_\beta}. \tag{5.28}$$

In combination with the expression for the group velocity, this gives $\hbar k^\alpha = m_{\alpha\beta}v^\beta$. Now, the LBE becomes

$$ev^\alpha \mathcal{E}_\alpha \frac{\partial f^0}{\partial E} + \frac{e}{\hbar}\epsilon_{\alpha\beta\gamma}v^\alpha B^\gamma A^\beta = \frac{m_{\alpha\beta}v^\alpha A^\beta(E)}{\hbar\tau}. \tag{5.29}$$

Dividing by the group velocity and multiplying by $\hbar$ gives

$$e\hbar\mathcal{E}_\alpha \frac{\partial f^0}{\partial E} = e\left[e\epsilon_{\alpha\beta\gamma}B^\gamma + \frac{m_{\alpha\beta}}{\tau}\right]A^\beta(E). \tag{5.30}$$

Rewriting gives an expression for the distribution function as

$$\delta f(\mathbf{k}) = \mathbf{k}\cdot\mathbf{A}(E) \tag{5.31}$$

$$= e\mathcal{E}_\beta v^\nu m_{\nu\alpha}\frac{\partial f^0}{\partial E}\left[e\epsilon_{\alpha\beta\gamma}B^\gamma + \frac{m_{\alpha\beta}}{\tau}\right]^{-1}. \tag{5.32}$$

It is now possible to write an explicit expression for the conductivity. The temperature is set to zero, so that the derivative of the Fermi-Dirac distribution becomes a negative delta function.

$$\sigma_{\xi\beta}(\mathbf{B}) = 2e^2\int_{E_f} v^\xi v^\nu m_{\nu\alpha}\left[e\epsilon_{\alpha\beta\gamma}B^\gamma + \frac{m_{\alpha\beta}}{\tau}\right]^{-1}\frac{d^3k}{(2\pi)^3}. \tag{5.33}$$

For higher temperatures, the integral would be over the entire Brillouin zone weighted by the Fermi-Dirac distribution.

5.3. Numerical approach

To improve the accuracy of magnetoresistance calculations, the LBE could be solved numerically without the relaxation time approximation. The equation to solve would then be

$$\frac{\partial\delta f(\mathbf{k})}{\partial t} - \frac{e}{\hbar}\boldsymbol{v}\times\mathbf{B}\cdot\frac{\partial\delta f(\mathbf{k})}{\partial\mathbf{k}} + \boldsymbol{v}\cdot\left[e\boldsymbol{\mathcal{E}} + \frac{E-\mu}{T}\nabla T\right]\left(-\frac{\partial f^0(\mathbf{k})}{\partial E}\right) = -\int\frac{d^3k}{(2\pi)^3}W_{\boldsymbol{k},\boldsymbol{k'}}[f(\boldsymbol{k}) - f(\boldsymbol{k'})]. \tag{5.34}$$

6. Method

Post-processing of the data from NEMO5 is done using MATLAB. NEMO5 outputs the band structure and the overlap between all states within a given energy range. MATLAB is used to calculate the derivatives for the group velocities and effective masses, and to perform the summations for the relaxation time and the conductivity.

6.1. Studied cases

Magnetoresistance calculations will be done for three cases. The first case corresponds to a sample without doping or gating. The surface potentials are fixed to zero volt and the Fermi level is at 0 eV. The second case is not physical, but can be used to explore the effect of bulk bands on the transport. The same band structure is used, but the Fermi level is chosen at 200 meV. The third case in unphysical as well. One of the surfaces is fixed at 0 V and the other at 0.5 V, while the Fermi level is chosen at 100 meV. Qualitative differences are to be expected. In the first case, only surface states contribute to the transport. In the other two cases, bulk bands contribute to the transport as well.

An alternative to choosing an artificial, higher Fermi level, would have been to increase the surface potentials until the bulk bands intersect with the Fermi level at 0 meV.

6.1.1. Energy tolerance

A state is considered to be at the Fermi level if its energy falls within a certain tolerance around it. The size of this tolerance should be zero ideally, since the assumption of zero temperature was made. In practice, it is limited by the finite grid density in the k_x–k_y plane. If the tolerance is too small, entire regions of the band structure drop out of the selection. It was found that a tolerance of ± 4 meV works well. Using $E = k_\mathrm{B}T$, this can be translated to a temperature of 46.4 K.

Unfortunately, increasing the grid density becomes expensive quickly. It is necessary to calculate the overlap of the wave functions between all sets of two states at the Fermi level. The number of overlap integrals thus equals the number of states at the Fermi level squared.

6.2. Parameter fitting

Not all quantities in the definition of the relaxation time, equation 5.19, are known. The first unknown is the Thomas-Fermi screening length ξ. It is estimated to lie between 1 nm and 10 nm.

Another unknown quantity is the impurity density n_{imp} of the material, which acts as a scaling factor for the relaxation time. Furthermore a volume is missing: the summation is the result of an integral over the Fermi surface. The volume of the Brillouin zone should thus be included. Rather than treating this separately, all scaling factors are included in one single scaling parameter:

$$n_{\text{scale}} = \frac{2\pi}{\hbar} V_{\text{BZ}} \left(\frac{e^2}{2\epsilon_0 \epsilon_r} \right)^2 n_{\text{imp}}. \tag{6.1}$$

The initial guess for n_{scale} will be made by choosing it such that the size of the relaxation time is realistic. It should be on the order of a tenth of a picosecond. Choosing n_{scale} too small or too large results matrices that are almost singular. After inversion, this leads to diverging or oscillating solutions for the magnetoresistance. Therefore, after the initial guess, the parameters will be fine tuned. A simple selection rule is that the conductivity σ_{xx} may not have a negative value, for that would mean that the current flows against the potential that induces it. After that, magnetoresistance is calculated for a small range of the two parameters. The results are fitted using a quadratic fit and a cubic natural spline. For each fit, a score is assigned to the solution.

For the quadratic fit, the relative error is determined. The score is the inverse of this error.

For the spline, the absolute value of its second derivative is integrated. The score is the inverse of the resulting value. It is a measure of the smoothness of the fit. A natural cubic spline was used because it is the smoothest fit through a set of points.

Together, these scores give a quick insight in where the magnetoresistance is smooth and does not diverge.

6.3. Practical difficulties

6.3.1. Infinite masses

States which are located in a part of the band structure with zero curvature have an infinite effective mass, according to equation 5.28. This is not physical; indeed, the equation is a result of local parabolic approximation of the band structure. In a parabolic band, the second derivative is never zero. Infinite masses give rise to numerical difficulties. To prevent this, the determinant of the Hessian matrix is corrected as

$$\text{Det} = \text{Det} \pm \epsilon \frac{\hbar^2}{m_e}. \tag{6.2}$$

The sign of the correction depends on the sign of the uncorrected determinant, for it must be steered away from zero. ϵ is taken to be 0.1. With this correction, the largest effective mass is set to 20 electron masses.

6.3.2. Different grids

Some difficulties arise when comparing the results of the different cases in the next section. Different grid densities are used for each case. That is done to get the best possible

resolution. The integral over the first Brillouin zone in equation 5.19 is calculated by summing over all the states. It needs to be multiplied by the volume of the Brillouin zone and divided by the number of grid points:

$$\frac{V_{\mathrm{BZ}}}{N}\sum_{n} = \int_{\mathrm{BZ}} d^3k \tag{6.3}$$

In the MATLAB code this is not done. The volume was included in the scaling parameter n_{scale}. However, the number of grid points was *not* included in the scaling parameter, because it depends on the grid.

A correction on n_{scale} is required to compare all cases. One of the grids was chosen as a reference grid, namely that of the second case, although the specific choice does not influence the results. Correction for the grid density is done by dividing by the relative grid density:

$$\hat{n}_{\mathrm{scale}} = n_{\mathrm{scale}}\frac{\text{grid density}_{\mathrm{ref}}}{\text{grid density}}. \tag{6.4}$$

In following results this correction is already done. The hat on the corrected scaling parameter will be omitted.

7. Results and discussion

This chapter presents the results of the magnetoresistance calculations. As discussed, there is no full agreement on the mechanism behind the positive linear magnetoresistance in Bi_2Te_3. It is interesting to see if the topological surface states, or the bulk states play the most important role. Three cases are compared to come to a conclusion.

One thing to keep in mind is that the relaxation time approximation was applied to solve the linearized Boltzmann equation. The use of this approximation can be justified in isotropic systems. For Bi_2Te_3, it will not give accurate quantitative results. Therefore, only the relative magnetoresistance is presented. The results in this chapter will hopefully give a picture of the magnetoresistance that is qualitatively correct.

The figures of the calculated magnetoresistance contain plots for various choices of the screening length ξ and the scaling parameter n_{scale}, which were defined in the previous chapters. The scaling parameter scales the magnitude of the relaxation time.

For each of the three cases, the total overlap is plotted. This is the overlap integral in the expression for the relaxation time, summed over all states on the Fermi surface:

$$\text{total overlap} = \sum_{\mathbf{k}',\mathbf{k}} |\left\langle \boldsymbol{\psi}(\boldsymbol{k'}) \middle| \boldsymbol{\psi}(\boldsymbol{k}) \right\rangle|^2. \tag{7.1}$$

Geometric information is lost since everything is summed. The resulting number gives an indication of the total coherence between all states. A slight increase can still be relevant as not all overlaps have the same weight in the summation for the relaxation time. For each value of the magnetic field, the total overlap was normalized by dividing by the number of states squared. It is an indication of the average overlap per state.

7.1. Zero boundary conditions

In these cases, the voltage at both surfaces is set to zero. The Fermi level is first chosen at 0 meV, and afterwards artificially chosen at 200 meV to include bulk conduction bands in the transport.

7.1.1. Dirac cone

The Fermi surface for the first case is similar to that of figure 2.4a. That surface was the result of just the Schrödinger solver, without the Poisson part. Here, the full Schrödinger-Poisson solver is used. The difference with the figure is that now, the two separate bands are shifted on top of one another. The slightly hexagonal shape remains the same.

No positive linear magnetoresistance is observed for a Fermi level that cuts only the Dirac cone. For some choices of n_{scale}, it is possible to obtain a smooth but strongly

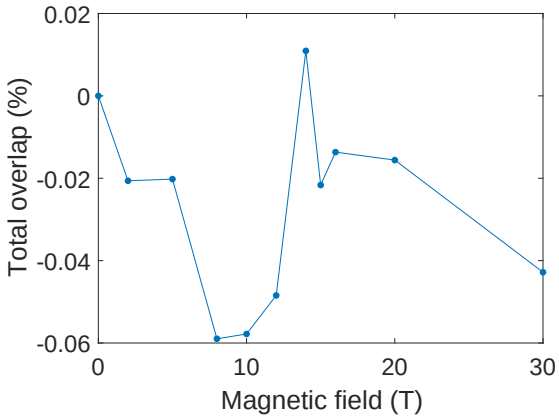

Figure 7.1.: Total overlap in the Dirac cone.

negative magnetoresistance, up to about -80% at a magnetic field of 20 Tesla. This relation is negative and strongly nonlinear. Magnetoresistance plots for these parameters are not shown. Figure 7.2 shows the magnetoresistance for the same parameters that are found and shown in section 7.1.2. It makes sense to compare the two cases for the same parameters, since both cases use the same band structure.

If the results are assumed to be correct, they indicate that the in literature observed positive, linear magnetoresistance is not purely a surface state effect. There might be some transport contribution from bulk states involved.

The possibility remains that the way the magnetic field is implemented in the tight-binding model gives the wrong result for the spin alignment. According to the model, the surface states do not align their spin with the magnetic field. Because the spins do not align, the total overlap in figure 7.1 changes hardly. The relaxation time is not changing with the magnetic field. If, in reality, the surface states do align their spin with a magnetic field, they might still give rise to positive linear magnetoresistance.

7.1.2. Conduction band

The same band structure is used, but with a Fermi level chosen at 200 meV. Two extra bulk conduction bands are involved in transport. Figure 2.4b shows the states at this energy. It makes sense to see if the bulk bands have an influence on the magnetoresistance, because they do align their spin with a magnetic field. The idea is that contributions of bulk bands will ensure that the overlap integrals increase significantly. Figure 7.3 shows that the total overlap indeed increases. Note the different scale on the y-axis compared to the case where only the surface states were involved. It is interesting to see that the total overlap is decreasing at first.

As an extra illustration, figure 7.4 shows the overlap between two different reference states and all other states on the Fermi surface. Both figures show two cases: no magnetic field, and a field of 20 T. The figure on the left has a reference in the Dirac cone. The magnetic field has no observable effect. The right figure takes a bulk state as reference.

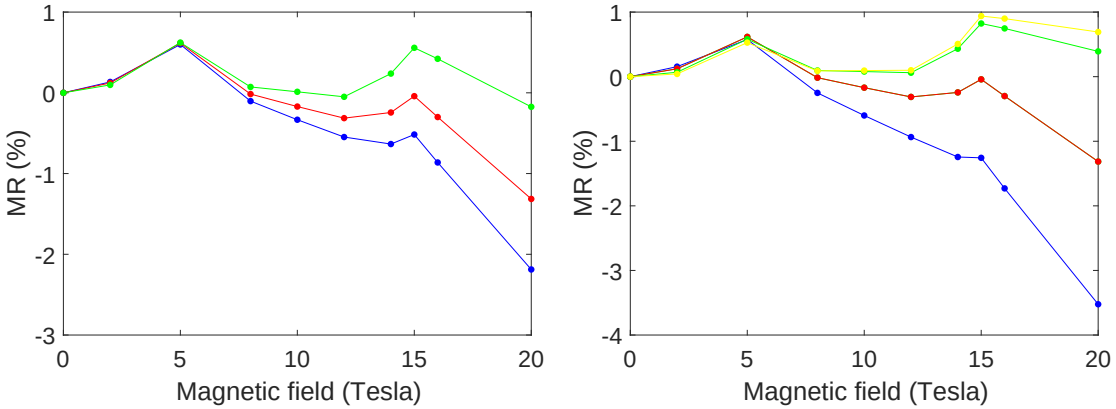

(a) $\xi = 2$, $n_{\text{scale}} = 1.3, 1.5, 2.0$ (b) $n_{\text{scale}} = 15$, $\xi = 1.5, 2.0, 4.0, 8.0$

Figure 7.2.: Magnetoresistance in the Dirac cone for different parameters.

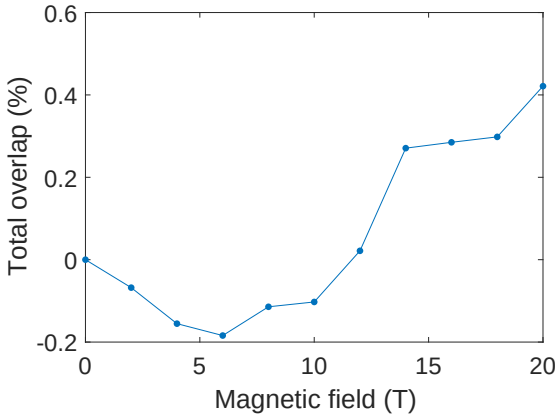

Figure 7.3.: Total overlap in the conduction band.

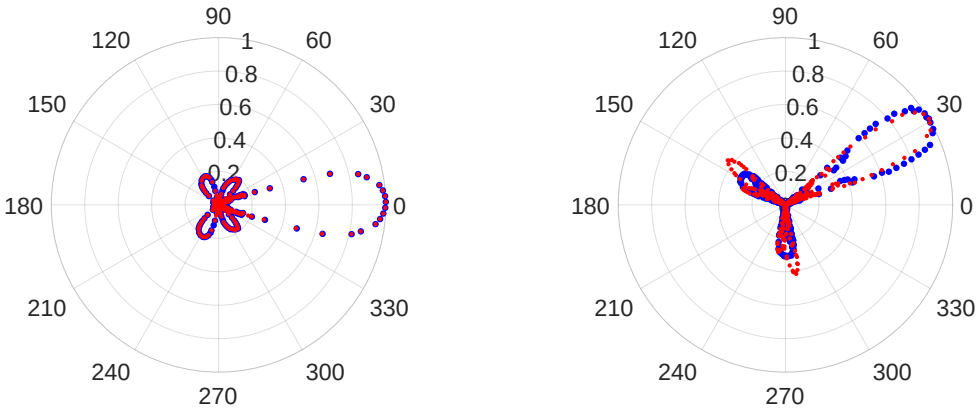

Figure 7.4.: Polar plots of the relative overlap between two reference states and all other states, for 0 T and 20 T. The distance from the origin corresponds to the magnitude of the overlap. The bulk-reference state is on the inner side of the oval from figure 2.4b

Here, the overlap is enhanced by the magnetic field. One can also see that the relative positions of the four smaller lobes change.

Figure 7.5 shows the resulting magnetoresistance. The increase in wave function overlap results clearly in a positive relation for specific values of ξ and n_{scale}. An increase of 23% at 20 T is the largest increase that was found. Other choices for ξ and n_{scale} can still cause diverging solutions.

7.2. Band bending

A positive potential of 0.5 V applied on one of the surfaces, and a Fermi level taken at 100 meV, results in the states shown in figure 2.4d. Gaps appear in some bands due to the energy tolerance around the Fermi level. More bulk bands are present compared to the previous case. One might, therefore, expect an even stronger magnetoresistance effect. The opposite turns out to be the case. A first indication is given by the total overlap in figure 7.6a. Once again it changes, significantly compared to the first case. However, instead of increasing, it decreases for stronger magnetic fields.

The values of ξ and n_{scale} that gave the strongest magnetoresistance for the previous case are used here as well. The result is shown as the blue plot in figure 7.6b. The red plot shows one of the smoothest solutions, found by varying the parameters slightly. Other parameters were tried as well. The magnetoresistance never becomes positive, except for diverging solutions.

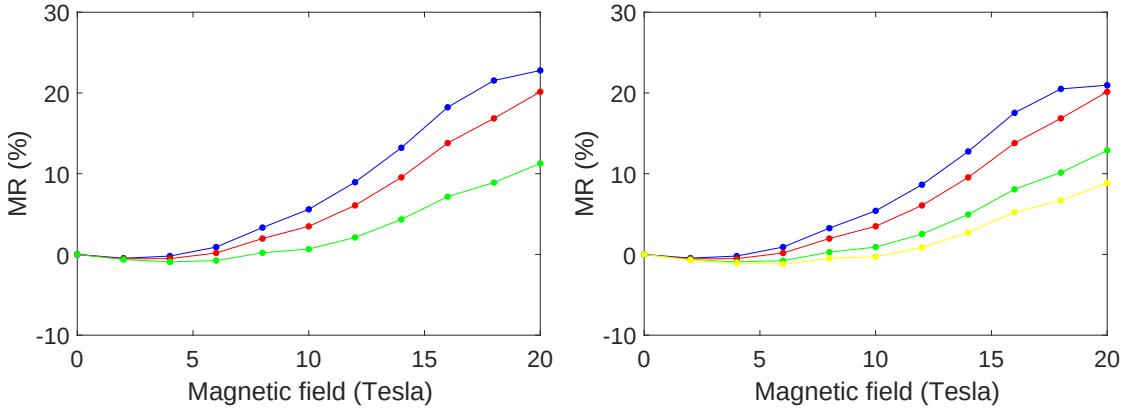

(a) $\xi = 2$, $n_{\text{scale}} = 1.3, 1.5, 2.0$

(b) $n_{\text{scale}} = 1.5$, $\xi = 1.5, 2.0, 4.0, 8.0$

Figure 7.5.: Magnetoresistance in the conduction band for different parameters.

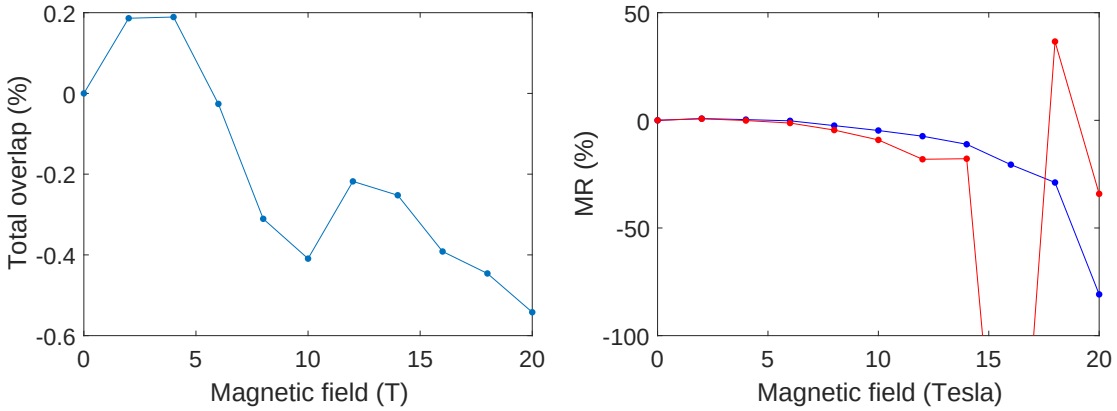

(a) Total overlap for the thin-film with an applied potential.

(b) $\xi = 2.0$, $n_{\text{scale}} = 1.3, 1.7$

Figure 7.6.: Total overlap and magnetoresistance for a potential difference of 0.5 V.

7.3. Discussion

It is hard to make a concluding statement about the validity of the results. The screening length ξ and the scaling factor n_{scale} are not known. Magnetoresistance plots that look physically plausible (not diverging) are found for screening factors that are physically plausible as well.

Some approximations are made in the derivation of the linearized Boltzmann equation, the most important ones being the relaxation time approximation and the parabolic band approximation. The relaxation time approximation replaces the collision integral with a simple expression that does not depend on the distribution function. The relaxation time approximation is exact for systems with isotropic bands and isotropic scattering. Its use for systems with anisotropic bands and anisotropic scattering is at best questionable[18]. The parabolic band approximation relates mass to the inverse of the curvature of the bands, which is valid for parabolic bands. To the author's knowledge, no better alternatives are available.

The linearized Boltzmann equation needs results from the band structure calculations. Any errors introduced there, whether numerical or more fundamental, will end up in the final result. A higher grid resolution could help to increase accuracy, but this becomes expensive in terms of computational cost. Mimicking the influence of doping by adsorbates is done by fixing the potential on the surfaces of the sample. NEMO5 has a specialized option for including surface passivation, which might be a more realistic treatment. However, this functionality depends on passivation parameters, for which the correct values are not known.

Part III.

Conclusion

8. Conclusion and outlook

8.1. Conclusion

Using a 20 orbital tight-binding Schrödinger-Poisson formalism, the band structure of 15 QL thin-film Bi_2Te_3 was calculated for various surface potentials and magnetic fields. Applying a positive potential on one of the surfaces pulls the conduction band down towards the Dirac cone. A negative potential pushes the valence band up. The potential landscapes for the two cases are not symmetric. The effects of the magnetic field on the band structure are not as expected. The effective g-factor is smaller than values reported in literature. This could not be explained and might be a shortcoming of the implementation of the tight-binding model in NEMO5. Meanwhile, the spins of almost all states align with a magnetic field. It is found that states in the Dirac cone refuse to align their spin with a magnetic field. It was shown that the Dirac cone opens for a thin-film of 6 QL, because of hybridization of the wave functions of the surface states.

Calculations of the relative magnetoresistance were performed by solving the linearized Boltzmann equation with the relaxation time approximation. Three different cases were treated. The first two calculations were done with the two surfaces of the thin-film fixed at 0 V. This system does not show positive magnetoresistance for a Fermi surface which includes only states from the Dirac cone. Choosing the Fermi level at 200 meV results in positive magnetoresistance for screening lengths close to 2 nm. In this case, the Fermi surface includes states from the Dirac cone and two bulk conduction bands. These conduction bands do align their spin with the magnetic field. A last calculation was done for a thin-film with a surface potential difference of 0.5 V. The conduction bulk bands are pulled down and the Fermi level was chosen to cut a large number of bands. This did not result in positive magnetoresistance.

Positive magnetoresistance in Bi_2Te_3 thin-films is predicted when the lowest bulk conduction bands contribute to the transport. The effects of a magnetic field on the band structure and spin alignment have yet to be fully understood. If the results are assumed to be correct, they indicate that the in literature observed positive, linear magnetoresistance is not purely a surface state effect.

8.2. Outlook

When continuing this project, the next step should be to validate experimentally that the surface states do not align their spin with an external magnetic field. This is important, because spin alignment is crucial for the magnetoresistance calculations. After that, it makes sense to continue with quantitative predictions for the magnetoresistance. To this end, the linearized Boltzmann equation should be solved without making the relaxation time approximation. This needs to be done using numerical methods.

A higher grid density for the band structure calculations will improve the accuracy of the magnetoresistance calculations as well. However, the computational cost increases rapidly as the grid density increases. Some way to interpolate wave functions could help to greatly reduce the computational cost, because then a smaller number of grid points could be used. The rotational symmetry of the Fermi surface could be exploited as well. The band structure is then solved only on a part of the grid. Somehow, the wave functions on the rest of the grid must be reconstructed.

Bibliography

[1] M. Z. Hasan and C. L. Kane. "*Colloquium* : Topological insulators". In: *Rev. Mod. Phys.* 82 (4 2010), pp. 3045–3067. DOI: 10.1103/RevModPhys.82.3045.

[2] Xiaolin Wang et al. "Room Temperature Giant and Linear Magnetoresistance in Topological Insulator Bi_2Te_3 Nanosheets". In: *Phys. Rev. Lett.* 108 (26 2012), p. 266806. DOI: 10.1103/PhysRevLett.108.266806.

[3] Hongtao He et al. "High-field linear magneto-resistance in topological insulator Bi2Se3 thin films". In: *Applied Physics Letters* 100.3, 032105 (2012). DOI: http://dx.doi.org/10.1063/1.3677669.

[4] Haijun Zhang et al. "Topological insulators in Bi2Se3, Bi2Te3 and Sb2Te3 with a single Dirac cone on the surface". In: *Nature Physics* 5.6 (2009), pp. 438–442. ISSN: 1745-2473. DOI: 10.1038/nphys1270.

[5] N.W. Ashcroft and N.D. Mermin. *Solid State Physics*. Philadelphia: Brooks/Cole, Cengage Learning, 1976.

[6] Seungwon Lee and Paul von Allmen. "Tight-binding modeling of thermoelectric properties of bismuth telluride". In: *Applied Physics Letters* 88.2, 022107 (2006). DOI: http://dx.doi.org/10.1063/1.2162863.

[7] Xiao-Liang Qi and Shou-Cheng Zhang. "Topological insulators and superconductors". In: *Rev. Mod. Phys.* 83 (4 2011), pp. 1057–1110. DOI: 10.1103/RevModPhys.83.1057.

[8] Charles Kane and Joel Moore. "Topological insulators". In: *Physics World* 24.02 (2011), p. 32.

[9] Kai Sun. *Lecture notes in Advanced Condensed Matter Physics*. 2013. DOI: http://www-personal.umich.edu/~sunkai/teaching/Fall_2013/phys620.html.

[10] D. P. Leusink et al. "Magnetoresistance from broken spin helicity". In: *arXiv* (2014).

[11] Sebastian Steiger et al. "NEMO5: A Parallel Multiscale Nanoelectronics Modeling Tool". In: *IEEE Transactions on Nanotechnology* 10 (6 2011), p. 1464. DOI: 10.1109/TNANO.2011.2166164.

[12] Alexandre Zimmer et al. "Characterizations of bismuth telluride films from Mott-Schottky plot and spectroscopic ellipsometry". In: *Surface and Interface Analysis* 40.3-4 (2008), pp. 593–596. ISSN: 1096-9918. DOI: 10.1002/sia.2715.

[13] P. Ngabonziza et al. "*In situ* spectroscopy of intrinsic Bi_2Te_3 topological insulator thin films and impact of extrinsic defects". In: *Phys. Rev. B* 92 (3 2015), p. 035405. DOI: 10.1103/PhysRevB.92.035405.

[14] Chao-Xing Liu et al. "Oscillatory crossover from two-dimensional to three-dimensional topological insulators". In: *Phys. Rev. B* 81 (4 2010), p. 041307. DOI: 10.1103/PhysRevB.81.041307.

[15] Hai-Zhou Lu et al. "Massive Dirac fermions and spin physics in an ultrathin film of topological insulator". In: *Phys. Rev. B* 81 (11 2010), p. 115407. DOI: 10.1103/PhysRevB.81.115407.

[16] P. Drath and G. Landwehr. "Band parameters and g-factor for n-type Bi2Te3 from the Schubnikow-De Haas effect". In: *Phys. Lett.* 24.10 (1967), pp. 504–506. DOI: 10.1016/0375-9601(67)90807-9.

[17] A. Wolos et al. "g-factors of conduction electrons and holes in Bi_2Se_3 three-dimensional topological insulator". In: *Phys. Rev. B* 93 (15 2016), p. 155114. DOI: 10.1103/PhysRevB.93.155114.

[18] D. I. Pikulin, Chang-Yu Hou, and C. W. J. Beenakker. "Nernst effect beyond the relaxation-time approximation". In: *Phys. Rev. B* 84 (3 2011), p. 035133. DOI: 10.1103/PhysRevB.84.035133.